Check for updates

The Meteoritical Society

Meteoritics & Planetary Science 1–36 (2026)
doi: 10.1111/maps.70246

Variably shock-compacted chondrites: Deformation–thermal histories, large differences in mineral deformation response, and implications for lithification

Alex M. RUZICKA[1]*, Jon M. FRIEDRICH[2,3], Richard C. HUGO[1], Robert J. MACKE[4], Daniel SHEIKH[1], and Melinda HUTSON[1]

[1]Cascadia Meteorite Laboratory, Portland State University, School of Earth, Environment and Society—Earth and Planetary Sciences Academic Area, Portland, Oregon, USA
[2]Department of Chemistry, Fordham University, Bronx, New York, USA
[3]Department of Earth and Planetary Sciences, American Museum of Natural History, New York, New York, USA
[4]Vatican Observatory, Vatican City State

***Correspondence**
Alex M. Ruzicka, Cascadia Meteorite Laboratory, Portland State University, School of Earth, Environment and Society—Earth and Planetary Science Academic Area, Portland, OR 97207-0751, USA
Email: ruzickaa@pdx.edu

(Received 26 April 2026; revision accepted 26 September 2026)

Abstract–Eight different H, L, and LL chondrites with 11 lithologies were studied and show good evidence for progressive shock effects and compaction. In weakly shocked chondrites (Baszkówka, Bjurböle, Saratov, NWA 7298 Lithology A and C), silicates were dominantly fractured, troilite and metal were more deformed than olivine and fluidized, and estimated stresses were ~4–7 GPa. In strongly shocked chondrites (NWA 7298 Lithology B, NWA 11315 Lithology A and B, Alfianello, NWA 8709, NWA 4860), olivine grains display more plastic deformation than in weakly shocked chondrites and were ultimately recrystallized; troilite, some metal, and some bulk areas were melted; and estimated stresses were >7 GPa. Three settings for lithification are inferred: (A) initial lithification during accretion of warm chondrule aggregates, (B) later lithification in warm, metamorphosing parent bodies that were being affected by mainly low-velocity collisions, and (C) final lithification in cool parent bodies after the waning of metamorphic heat that were being affected by higher velocity collisions. Thus, collisions together with heat of different types (accretionary, metamorphic, and shock-related) were probably the main ways in which unmelted planetesimals were lithified. Impact-fluidized metal and troilite may have acted as important lithification binding agents even in weak shock events.

INTRODUCTION

A critical step in planet formation was the formation of planetesimals that were lithified to form the first rocky bodies. How such lithification occurred is not well understood. The earliest formed rocks whose textures were not destroyed by large-scale melting are chondrites. Thus, primordial lithification processes are amenable to study with chondrites that formed in planetesimals. Although details are uncertain, the consensus is that shock compaction was important in decreasing the porosities of chondrites and chondritic planetesimals (Beitz et al., 2013, 2016; Bland et al., 2011, 2014; Collins et al., 2019; Consolmagno et al., 1998; Consolmagno & Britt, 2004; Forman et al., 2016; Friedrich, Rubin, et al., 2014; Hanna et al., 2015). This implies that shock compaction could have been important for lithification.

However, shock compaction can involve competing effects that would either assist or hinder lithification, and little assessment has been made to date of the importance of these different effects for chondrites. On a small scale, fracturing and cataclasis will create fragments and voids to

© 2026 The Author(s). *Meteoritics & Planetary Science* published by Wiley Periodicals LLC on behalf of The Meteoritical Society.
This is an open access article under the terms of the Creative Commons Attribution License, which permits use, distribution and reproduction in any medium, provided the original work is properly cited.

inhibit lithification, but porosity also could have localized deformation and heating that would promote lithification near pores (Bland et al., 2014; Collins et al., 2019; Kieffer, 1975). In general, impact compression will promote lithification by forcing materials together and removing porosity and by binding materials together with shock-generated heat by annealing (sintering), melting, or the creation of new grains (Bischoff et al., 1983; Hörz et al., 2005; Kieffer, 1975; Nakamura et al., 2000; Spray, 2016). On a larger scale, impact cratering events on low-gravity planetesimals will erode or destroy bodies by fragmentation if impact velocities exceed a threshold (Hartmann, 1979; Holsapple et al., 2002; Stewart & Leinhardt, 2009; Stöffler et al., 1988), but ejecta and remnants can re-accrete (forming a "rubble pile") and this might allow impact-disrupted bodies to grow or form again possibly with a different porosity structure (Beitz et al., 2016; Melosh & Ryan, 1997; Michel et al., 2001; Scheeres et al., 2002). Another variable of possible importance is the thermal state of planetesimals during collisional events. If planetesimals were warm when impacted this could have affected the cratering process (Ciesla et al., 2013) and could have facilitated lithification through annealing, softening, or melting. There is evidence that some ordinary chondrites were shocked while warm (e.g., Ruzicka et al., 2005, 2015) and that ordinary chondrite parent bodies were disrupted, reassembled, and re-impacted while warm (Blackburn et al., 2017; Grimm, 1985; Rubin, 2025, 2026; Taylor et al., 1987).

In this study, we examine a suite of H, L, and LL chondrites that appear to illustrate the effects of progressive shock effects and compaction. We had different goals: (1) assess the relationship of plastic deformation in olivine with bulk properties including porosity and 3-D metal fabric data using quantitative metrics; (2) evaluate deformation features in each meteorite using petrographic and SEM data to better constrain temperature during shock, deformation intensity, and annealing histories; (3) compare deformation features in different key minerals for a more comprehensive study of shock effects; (4) evaluate the role that collisions may have played in the lithification of chondrites.

Techniques utilized here include optical petrography, bulk porosity determinations using ideal-gas pycnometry, X-ray microtomography (μCT), as well as an emphasis on electron backscatter diffraction (EBSD) and accompanying scanning electron microscopy (SEM). Focus is placed on three different key minerals, including olivine, FeNi-metal, and troilite, chosen for different reasons: (1) Olivine is the most abundant mineral in chondrites and in the terrestrial upper mantle and its deformation behavior consequently has been well studied (e.g., Gueguen & Nicolas, 1980; Karato et al., 2008; Ruzicka et al., 2024; Stöffler et al., 1988, 1991); (2) FeNi-metal in bulk chondrite samples (body centered cubic [bcc] alloy is the chief metallic mineral in chondrites) has been studied with μCT and magnetic anisotropy and often shows a fabric that has been interpreted to reflect shock compaction (Friedrich et al., 2017; Friedrich, Wignarajah, et al., 2008; Gattacceca et al., 2005; Krzesińska et al., 2015; Macente et al., 2025; Sneyd et al., 1988); and (3) troilite is known to deform very differently during shock depending on pre-shock temperature (Schmitt, 2000). We show here that the three minerals have different responses to shock and that this can be used to assess deformation and lithification conditions.

SAMPLES AND METHODS

Samples

Table 1 lists the samples that were studied, which include H, L, and LL chondrites known to represent a variety of shock stages, porosities, and metal textures (e.g., Friedrich et al., 2017). Baszkówka (LL5), Saratov (L4), and Bjurböle (L/LL4) are all weakly shocked and notably porous (Friedrich et al., 2017); Northwest Africa (NWA) 11351 is a strongly shocked LL3-5 genomict breccia with three lithologies (Ruzicka et al., 2024), two of which were studied here (A, B); Alfianello (L6) is strongly shocked; NWA 8709 is a strongly shocked L3 melt breccia (Ruzicka et al., 2020); and NWA 4860 is a strongly shocked (Schepker, 2014) L4 melt breccia.

NWA 7298 is a genomict breccia with three variably shocked lithologies (Lithology A, B, C) that was classified as an H3-4 (Friedrich, Weisberg, et al., 2014), but current data suggest that it is better described as an H3-5. Lithology C was suggested to be type 3, but it is texturally integrated, and EBSD suggests a mineralogy more consistent with a type 5 designation (see Huss et al., 2006 for metamorphism-related type characteristics), with most low-Ca pyroxene as orthopyroxene (opx) and little as clinoenstatite (clen) (clen/[clen+opx] ~0.01 area fraction) and containing notable amounts of plagioclase (~1 area% for >10 μm diameter grains). This compares to Lithology A and Lithology B, which have more clinoenstatite and less plagioclase, and which could be type 3 or type 4 (Lithology A: clen/[clen+opx] ~0.13–0.14, ~0.3–0.7 area % plagioclase; Lithology B: clen/[clen+opx] ~0.49, ~0% plagioclase). Lithology A, the host of NWA 7298 that encloses the other two lithologies (Lithology B and C) as clasts, appears to be a mixture of more equilibrated (type 5-like) and less equilibrated (type 3-like) material.

Methods

Four different experimental techniques were used, including (1) optical microscopy using a Leica DM2500

19455100, 0, Downloaded from https://onlinelibrary.wiley.com/doi/10.1111/maps.70246 by ALEX RUZICKA , Wiley Online Library on [09/11/2026]. See the Terms and Conditions (https://onlinelibrary.wiley.com/terms-and-conditions) on Wiley Online Library for rules of use; OA articles are governed by the applicable Creative Commons License

TABLE 1. Samples studied.

Meteorite	Group & type[a]	Weathering grade[a]	Fall/Find[a]	Sample designations[b]
Baszkówka	L5	W1	Fall	***CML0151-2***
Saratov	L4	W1	Fall	CML0057-1, ***CML0057-7***
Bjurböle	L/LL4	W1	Fall	CML0863-1, ***CML0863-2B***
Northwest Africa 7298	H3-5[c] genomict br.	W2	Find	***AMNH NWA7298,1*** & ***AMNH NWA7298,2***
Northwest Africa 11,351	LL3-6[d] genomict br.	W1	Find	CML0754-1, ***CML0754-2***
Alfianello	L6	W2	Fall	CML0496-1, ***CML0496-1A***
Northwest Africa 8709	L3 melt br.	W3	Find	CML0109-5C, *CML0109-2*, ***CML0109-5D***
Northwest Africa 4860	L4 melt br.	W1	Find	CML0288-2, *CML0288-3*, ***CML0288-5***

[a]Data from MBD (2026) except for weathering grade for Bjurböle and Saratov, which are estimated here. melt br. = melt breccia, genomict br. = genomict breccia.
[b]Italicized samples are polished thin sections (bolded italics are samples studied with EBSD and OM, non-bolded italics are samples studied by OM), non-italicized are bulk samples. CML = Cascadia Meteorite Laboratory sample numbers, AMNH = American Museum of Natural History sample numbers.
[c]Friedrich, Weisberg, and Rivers (2014) list Lithology A (host) as H3.8, Lithology B (clast) as H4, and Lithology C (clast) as H3 but in the samples examined here, Lithology C is equilibrated and resembles a type 5 chondrite.
[d]NWA 11351 Lithology A is LL3/4 with strong cluster texture, Lithology B is LL3/4 with poor cluster texture, Lithology C is an LL5-6 breccia (Ruzicka et al., 2024).

petrographic microscope to determine conventional shock stages (CSS; Stöffler et al., 1991, 2018, 2019) and weighted shock stages (WSS; Jamsja & Ruzicka, 2010; Ruzicka et al., 2015); (2) scanning electron microscopy (SEM) and electron backscatter diffraction (EBSD) to study textures and crystallography using equipment and methods similar to those used previously (Hugo et al., 2020; Ruzicka et al., 2024; Ruzicka & Hugo, 2018); (3) ideal gas pycnometry and optical laser scanning of bulk samples to determine bulk density, grain density, and porosity (Macke, 2010; Macke et al., 2015); and (4) X-ray microtomography (μCT) to study the three-dimensional shapes and orientations of metal grains in bulk samples (Friedrich, Wignarajah, et al., 2008).

For the optical microscopy work, CSS was determined from WSS by applying the "25% rule" in which CSS is the maximum shock stage shown by at least 25% of the grains (Stöffler et al., 1991, 2019). Olivine recrystallization was equated to an S6 shock stage (Bischoff et al., 2019; Fritz et al., 2017; Jamsja & Ruzicka, 2010). This makes the implicit assumption that recrystallization textures (undeformed granular grains meeting in triple junctions) were directly caused by shock deformation, either through static recrystallization driven by high dislocation densities and high post-shock temperatures (Druiventak et al., 2012) or dynamic recrystallization processes occurring during deformation (Lloyd et al., 1997).

Bulk porosity was not measured for NWA 7298, and instead the porosity of its three lithologies in a thin section (AMNH NWA 7298,1) was estimated in a single image mosaic (map LAM1-2, blended image EDS + FSD, where EDS = energy-dispersive spectrometer 9-element [Ni, Fe, Cr, Ca, S, P, Si, Al, Mg] false color map and FSD = forescatter diode image), equating black areas to voids and using ImageJ software with Color Inspector plug-in and WuQuant display to quantify the area proportion. The mapping approach used here is probably a good estimate of the relative (if not bulk) porosities of the lithologies, as the same SEM operating conditions apply and section were used.

Many EBSD map datasets were obtained, including large area maps (LAMs), detailed maps (DMs, formerly known as "mini-LAMs"—Ruzicka et al., 2024), and targeted maps (TMs). LAMs have the most area coverage (here operationally defined as $>25\,mm^2$) and contain many pixels (1.6–30.7 MP); DMs have regional coverage, a smaller step size to detect smaller features, and contain many pixels (2.8–18.1 MP); and TMs are mainly 1-field maps with fewer pixels and small areas of targeted or random locations. Both LAMs and DMs were used to obtain map-averaged EBSD deformation parameters. Metadata for EBSD maps (designations, number of fields, step sizes, map areas, map pixels, acquisition date) are given in Table S1 (Supplemental Material).

EBSD-SEM map images shown in this paper include layered images with a monochrome layer and a color layer. The monochrome layer represents all areas of the map and can include band contrast (BC); electron (simulated BSE image from an SE signal with an imposed negative bias current); or forescatter diode (FSD) (using an FSD detector signal). The color layer can include data for one or more phases such as $IPF_{x,y,z}$ inverse pole figure, which shows unit cell directions in sample X (left-right), Y (top-down), or Z (normal to section) coordinates; GOS (grain orientation spread, the average misorientation within a grain); GROD angle (grain reference orientation

19455100, 0, Downloaded from https://onlinelibrary.wiley.com/doi/10.1111/maps.70246 by ALEX RUZICKA , Wiley Online Library on [09/11/2026]. See the Terms and Conditions (https://onlinelibrary.wiley.com/terms-and-conditions) on Wiley Online Library for rules of use; OA articles are governed by the applicable Creative Commons License

deviation angle, the angular deviation within a crystal from the mean crystal orientation); or grain boundaries, including low angle or subgrain boundaries (<15° misorientation) or high angle grain boundaries (>15° misorientation).

Although EBSD data acquisition, processing, and analysis largely followed that of Ruzicka et al. (2024), some new methods were used. (1) Oxford Instruments AZtecCrystal software (most recent version 3.1) was used to fully remove data for grains below a threshold size (<5 pixels) in a denoising procedure (creating a new subset). The 5-pixel threshold was used previously to define grains, but pixel-based data products for grains below the threshold are not removed unless a new grain list is created that specifically excludes grains below the threshold. Crystal rotation axis (CRA) data for intragranular disorientations, including $R_{2\text{-}10}$ values and model deformation temperatures (T_{deform}) for olivine (Ruzicka et al., 2024), can be changed somewhat by denoising (e.g., 10–20 °C shifts in T_{deform} are common). Denoising also tends to improve the image quality of certain EBSD maps (e.g., phase, IPF orientation). (2) Special attention was given to the presence of features that could be related to recrystallization or recovery. Recrystallized grains are weakly deformed, equant grains that are separated from other grains by high angle grain boundaries (HAGBs, >15° disorientation) with various rotation axis/angles (as opposed to twins that have specific orientation relationships). In principle, recrystallization can be produced either by dynamic recrystallization (recrystallization during deformation) or static recrystallization (recrystallization during static heating following deformation) (Lloyd et al., 1997). Recovery features are taken to be low angle grain boundaries (LAGBs, <15° disorientation, i.e., subgrain boundaries) that are notably curved, as opposed to straight subgrain boundaries that occur in more deformed grains and were produced by deformation. (3) CRA diagrams, disorientation charts, and misorientation profiles were used to characterize twins in body-centered-cubic (bcc) metal and troilite.

Table S2 in the supplement provides a list of acronyms and abbreviations used in this work.

RESULTS

Bulk Properties and Deformation Intensity

Table 2 provides data for bulk samples based on pycnometry and sample shapes and μCT data for metal grains. Table 3 gives shock stage data based on optical microscopy and map-averaged EBSD data for deformation and grain size parameters. Figure 1 shows various parameters plotted against average grain orientation spread (GOS) for larger olivine grains with equivalent diameters (d) > 50 μm. GOS is a useful EBSD metric for plastic deformation (Brewer et al., 2009) but depends on grain size (Hugo et al., 2020; Ruzicka et al., 2024; Ruzicka & Hugo, 2018); average $GOS_{d>50}$ for olivine is especially useful because such larger grains are also used for optical shock stage analysis (Stöffler et al., 1991), and it is used here as the main parameter for shock intensity.

Figure 1a shows a nearly 1:1 correlation between olivine $GOS_{d>50}$ and weighted shock stage (WSS). This resembles the results of Ruzicka and Hugo (2018) and Ruzicka et al. (2024) for type 3 and 6 ordinary chondrites. The data suggest a rule-of-thumb in which *the value of average olivine $GOS_{d>50}$ (in degrees) in shocked chondrites corresponds roughly to the weighted shock stage*. This will be true so long as olivine is not significantly recrystallized, because recrystallization lowers GOS and increases WSS (Hugo et al., 2020; Ruzicka et al., 2024). Significant recrystallization of olivine is indicated by the "R" label in Figure 1 and is applied to NWA 4860 and NWA 8709. The former meteorite is more strongly recrystallized, which accounts for its displacement to the upper left of NWA 8709 in Figure 1a. Even so, these two meteorites with significant olivine recrystallization are not much removed from the overall 1:1 trend between WSS and average olivine $GOS_{d>50}$.

GOS is grain size dependent, as shown for olivine in Figure 1b (two size bins) and Table 3 (four size bins). In Figure 1b, there is a good correlation between olivine average $GOS_{d15\text{-}50}$ and $GOS_{d>50}$, with values being similar in less deformed meteorites and GOS values being notably lower for the smaller grains in more deformed meteorites. Thus, although GOS values in smaller (d < 50 μm) grains are related to shock intensities, *the nearly 1:1 correlation between WSS and GOS is strictly valid only for larger (d > 50 μm) grains.*

Figure 1c shows the relationship between porosity and olivine $GOS_{d>50}$. There is an overall inverse trend. Compared to the overall trend, the porosity of Alfianello is somewhat elevated. Moreover, weakly shocked samples (which have CSS = S1-S2 and WSS = 1.07–1.79) have large changes in porosity (from ~20%–8%) with no obvious accompanying change in average olivine $GOS_{d>50}$ values (~1.38° ± 0.52°) (Figure 1c, Tables 2 and 3). Despite scatter, however, the overall inverse trend between bulk porosity and shock intensity as given by olivine GOS is unmistakable. An inverse correlation between porosity and shock state in chondrites has long been noted (Consolmagno & Britt, 2004; Consolmagno et al., 1998).

The strength parameter C measures the anisotropy of grain shapes in 3-D data (Woodcock & Naylor, 1983).

19455100, 0, Downloaded from https://onlinelibrary.wiley.com/doi/10.1111/maps.70246 by ALEX RUZICKA , Wiley Online Library on [09/11/2026]. See the Terms and Conditions (https://onlinelibrary.wiley.com/terms-and-conditions) on Wiley Online Library for rules of use; OA articles are governed by the applicable Creative Commons License

TABLE 2. Density, porosity, and metal fabric data for bulk samples. Uncertainties given in parentheses.

Meteorite	Mass (g)	Bulk density (g/cm^3)	Grain density (g/cm^3)	Porosity (%)[a]	Metal fabric, number of grains	Metal fabric parameter, C (anisotropy strength)	Metal fabric parameter, K (lineation 1 ↔ foliation 0)	Metal fabric parameter, T (lineation −1 ↔ +1 planar)
Baszkówka	–	2.86 (0.05)[d]	3.54 (0.10)[d]	18.9 (0.5)[d]	–	0.12 (0.10)[e]	–	–
Saratov	13.04	3.04 (0.02)	3.63 (0.04)	16.3 (1.0)	–	0.310 (0.040)[e]	–	–
Bjurböle	7.00	2.83 (0.02)	3.56 (0.04)	20.4 (1.0)	–	0.294 (0.025)[e]	–	–
NWA 7298								
Lithology A	–	–	–	8.2	–	0.28[f]	–	–
Lithology B	–	–	–	2.6	–	0.78[f]	–	–
Lithology C	–	–	–	11.4	–	0.19[f]	–	–
NWA 11351[b]								
Lithology A	21.82	3.34 (0.01)	3.51 (0.02)	5.1 (0.7)	11,640	0.874	0.47	0.35
Lithology B					10,077	0.955	0.21	0.66
Lithology C					747	0.862	0.47	0.37
Alfianello	9.67	3.19 (0.02)	3.60 (0.05)	11.5 (1.5)	–	1.135[e]	–	–
NWA 8709[c]	2.16	3.22 (0.05)	3.35 (0.05)	4.1 (2.1)	5655	0.68	–	–
NWA 4860	20.47	3.31 (0.04)	3.50 (0.02)	5.6 (1.4)	3302	0.688	0.198	0.670

[a]Porosity values based on pycnometry and sample volumes except for NWA 7298, which were based on void spaces observed in thin section (area % assumed equivalent to vol%).
[b]Fabric data from Ruzicka et al. (2024).
[c]Data from Ruzicka et al. (2020).
[d]Data from Friedrich, Wignarajah, et al. (2008) (average of three measurements, standard deviations given in parentheses).
[e]Literature data (data and sources given in Friedrich et al. (2017), average values with standard deviations given in parentheses).
[f]Data from Friedrich, Weisberg, et al. (2014).

For μCT data of metal in chondrites, the value of C is related to metal grain long-axis alignment that manifests as a shape preferred orientation (SPO)—typically a foliation of grain long axes—and this SPO tends to be correlated with shock stages (Friedrich et al., 2017; Friedrich, Wignarajah, et al., 2008). Figure 1d similarly shows a rough correlation between metal C and olivine GOS. In detail, there is a bimodal distribution in Figure 1d, with a low-C-GOS group (Baszkówka, Saratov, Bjurböle, NWA 7298 Lithology A, NWA 7298 Lithology C), and a high-C-GOS group (NWA 11351 Lithology A, NWA 11351 Lithology B, Alfianello, NWA 7298 Lithology B, NWA 4860, NWA 8709). Also notable in Figure 1d is that for the high-C-GOS group, strength parameter C reaches a maximum for Alfianello and decreases as olivine GOS increases further.

In general, however, *the data for chondrites in this study are consistent with them having experienced variable compaction related to differences in the intensity of shock deformation*. Weakly shocked meteorites (Bazkówka, Saratov, Bjurböle, and Lithology A and C for NWA 7290) have higher porosity and lower metal SPO, whereas strongly shocked meteorites (NWA 11351 Lithology A and B, Lithology B of NWA 7290, NWA 8709, and NWA 4860) have lower porosity and higher metal SPO. The meteorites in this study therefore generally conform to a simple model of shock compaction (Friedrich et al., 2017).

Petrographic Features

Petrographic features provide important evidence for deformation styles and processes. In this section, meteorite lithologies are described roughly in order of increasing shock intensities as given by olivine GOS and WSS. Figure 2 shows SEM and EBSD images of weakly shocked lithologies (Baszkówka, Saratov, Bjurböle, NWA 7298 Lithology A), and Figure 3 shows images for strongly shocked lithologies (NWA 11315 Lithology A, Alfianello, NWA 8709, NWA 4860).

19455100, 0, Downloaded from https://onlinelibrary.wiley.com/doi/10.1111/maps.70246 by ALEX RUZICKA , Wiley Online Library on [09/11/2026]. See the Terms and Conditions (https://onlinelibrary.wiley.com/terms-and-conditions) on Wiley Online Library for rules of use; OA articles are governed by the applicable Creative Commons License

TABLE 3. Shock stage and map-averaged EBSD deformation parameters for olivine, bcc metal, and troilite.

Parameter[a]	Baszkówka	Saratov	Bjurböle	NWA 7298 Lithology A	NWA 7298 Lithology C	NWA 7298 Lithology B	NWA 11351 Lithology A	NWA 11351 Lithology B	Alfianello	NWA 8709	NWA 4860
PTS	CML0151-2	CML0057-7	CML0863-2C (OM) & CML0863-2B (OM, EBSD)	AMNH 7298,1 & AMNH 7298,2	AMNH 7298,1 & AMNH 7298,2	AMNH 7298,1	CML0754-2	CML0754-2	CML0496-1A	CML0109-2 (OM) & CML0109-5D (OM, EBSD)	CML0288-3 (OM) & CML0288-5 (OM, EBSD)
CSS	S1	S1	S1	S1	S2	S4	S4	S4	S5	S5	S6
CSS modes (%)	91 S1, 7 S2	65 S1, 23 S2	55 S1, 21 S2	68 S1, 21 S2	52 S1, 28 S2	59 S4, 20 S5	65 S4, 21 S3	59 S4, 18 S5	66 S4, 26 S5	52 S4, 30 S5	75 S6, 24 S5
WSS	1.07 (0.26)	1.49 (0.76)	1.79 (1.03)	1.44 (0.73)	1.72 (0.88)	3.96 (0.72)	3.76 (0.76)	3.87 (0.81)	4.17 (0.56)	4.62 (0.78)	5.74 (0.47)
N	58	155	115	129	52	49	66	79	131	71	85
EBSD map data averaged	LAM, DM1, DM2	LAM, DM	LAM, DM1, DM2	LAM1-1, LAM1-2	LAM1-2, LAM2	LAM1-1	LAM, DM1, DM2	LAM, DM2	LAM1, LAM2	LAM2, DM1, DM2	LAM, DM1, DM2
Total EBSD map area (mm^2)	132.2	64.7	89.5	132.3	113.8	71.3	90.7	30.7	85.5	69.0	39.1
Olivine											
$GOS_{d>50}$ (°)	0.85 (1.07) ± 0.06	1.77 (1.97) ± 0.59	1.73 (1.81) ± 0.13	1.36 (1.33) ± 0.10	1.90 (1.76) ± 0.09	4.61 (2.43)	3.22 (1.39) ± 0.62	3.29 (1.23) ± 0.15	4.33 (1.73) ± 0.06	6.62 (2.70) ± 0.80	5.28 (2.58) ± 0.31
$Sk_{d>50}$	1.91 ± 0.14	1.82 ± 0.19	1.58 ± 0.13	1.54 ± 0.17	1.54 ± 0.11	1.11	1.08 ± 0.01	1.07 ± 0.01	1.08 ± 0.01	1.11 ± 0.10	0.997 ± 0.014
Mean d d > 50 (μm)	96.4	84.5	83.8	79.6	86.2	84.6	87.5	76.1	96.0	86.1	76.8
Ng d > 50	1638	1221	1627	1303	1868	875	1284	442	2580	737	441
GOS_{d15-50} (°)	0.72 (0.97) ± 0.07	1.56 (1.73) ± 0.18	2.16 (1.90) ± 0.10	1.53 (1.54) ± 0.00	1.52 (1.64) ± 0.19	3.69 (2.23)	2.84 (1.50) ± 0.73	3.05 (1.43) ± 0.34	3.71 (1.90) ± 0.02	5.45 (2.83) ± 0.62	3.03 (2.76) ± 0.11
Sk_{d15-50}	1.93 ± 0.11	1.84 ± 0.11	1.34 ± 0.04	1.60 ± 0.02	1.78 ± 0.00	1.15	1.12 ± 0.02	1.10 ± 0.01	1.13 ± 0.02	1.05 ± 0.13	1.05 ± 0.20
Mean d d = 15–50 (μm)	23.9	24.6	23.9	23.6	24.5	24.1	23.8	23.3	26.2	23.8	22.7
Ng d = 15–50	12,786	7944	14,669	14,641	13,725	7214	9987	5400	9621	5533	8068
GOS_{d5-15} (°)	0.65 (0.89) ± 0.06	1.34 (1.45) ± 0.23	2.23 (1.83) ± 0.13	1.46 (1.56) ± 0.06	1.32 (1.55) ± 0.27	3.12 (1.97)	2.29 (1.35) ± 0.72	2.96 (1.55) ± 0.34	3.22 (1.89) ± 0.01	3.61 (2.82) ± 0.58	2.00 (2.18) ± 0.15
Sk_{d5-15}	1.93 ± 0.15	1.85 ± 0.07	1.25 ± 0.00	1.84 ± 0.02	2.10 ± 0.02	1.17	1.14 ± 0.02	1.11 ± 0.01	1.11 ± 0.01	1.33 ± 4.58	2.43 ± 1.74
Mean d d = 5–15 (μm)	8.6	10.2	8.7	11.9	11.9	11.9	9.0	9.7	9.8	11.2	8.6
Ng d = 5–15	51,839	15,854	49,317	22,294	16,321	10,131	32,956	15,612	11,457	7945	43,435
$GOS_{d<5}$ (°)	0.55 (0.75) ± 0.05	0.82 (0.87)	1.53 (1.50)	–	–	–	1.75 (1.08) ± 0.96	–	2.19 (1.50)	1.33 (1.52) ± 0.70	1.08 (1.54) ± 0.06
$Sk_{d<5}$	1.68 ± 0.18	1.63	1.68	–	–	–	1.17 ± 0.02	–	1.13	1.93 ± 0.12	2.88 ± 0.09
Mean d d < 5 (μm)	3.8	3.1	2.9	–	–	–	4.2	–	3.2	1.8	3.0

19455100, 0, Downloaded from https://onlinelibrary.wiley.com/doi/10.1111/maps.70246 by ALEX RUZICKA , Wiley Online Library on [09/11/2026]. See the Terms and Conditions (https://onlinelibrary.wiley.com/terms-and-conditions) on Wiley Online Library for rules of use; OA articles are governed by the applicable Creative Commons License

TABLE 3. *Continued.* Shock stage and map-averaged EBSD deformation parameters for olivine, bcc metal, and troilite.

Parameter[a]	Baszkówka	Saratov	Bjurböle	NWA 7298 Lithology A	NWA 7298 Lithology C	NWA 7298 Lithology B	NWA 11351 Lithology A	NWA 11351 Lithology B	Alfianello	NWA 8709	NWA 4860
Ng d < 5	21,296	25,467	50,851	–	–	–	18,155	–	15,988	42,609	50,869
$Sk_{d>50}/Sk_{d5\text{-}15}$	0.989 ± 0.107	0.988 ± 0.108	1.26 ± 0.10	0.836 ± 0.093	0.733 ± 0.055	0.950	0.948 ± 0.022	0.963 ± 0.010	0.980 ± 0.008	0.834 ± 2.882	0.411 ± 0.295
$Sk_{d15\text{-}50}/Sk_{d5\text{-}15}$	1.00 ± 0.10	1.00 ± 0.07	1.07 ± 0.03	0.871 ± 0.017	0.850 ± 0.009	0.989	0.980 ± 0.025	0.983 ± 0.011	1.01 ± 0.02	0.790 ± 2.728	0.433 ± 0.322
$Sk_{d<5}/Sk_{d5\text{-}15}$	0.871 ± 0.113	0.884 ± 0.034	1.34 ± 0.00	–	–	–	1.02 ± 0.03	1.02 ± 0.01	1.03 ± 0.01	1.46 ± 5.03	1.18 ± 0.85
$R_{2\text{-}10}$	0.590 ± 0.008	0.639 ± 0.023	0.598 ± 0.016	0.664 ± 0.006	0.637 ± 0.002	0.671	0.428 ± 0.040	0.443 ± 0.056	0.417 ± 0.037	0.479 ± 0.057	0.491 ± 0.046
T_{deform} (°C)	909 [90] ± 9	961 [88] ± 25	917 [90] ± 18	989 [86] ± 6	960 [88] ± 2	997 [86]	732 [99] ± 44	748 [98] ± 62	719 [99] ± 41	788 [96] ± 87	800 [95] ± 50
Np 2–10 CRA	160,771	134,292	631,832	125,213	161,142	344,628	1,005,836	476,516	2,575,287	618,023	899,880
Metal (bcc)											
$GOS_{d15\text{-}50}$ (°)	3.76 (1.22) ± 0.58	6.33 (3.57) ± 0.44	5.92 (2.53) ± 0.76	9.44 (3.48) ± 1.05	11.6 (4.1) ± 1.2	7.80 (3.54)	5.94 (2.40) ± 1.32	5.33 (1.66) ± 1.19	1.29 (1.50) ± 0.43	4.08 (2.31)	5.68 (1.45) ± 0.41
Mean d d = 15–50 (μm)	23.6	24.1	24.6	25.1	24.3	27.0	23.1	24.0	25.6	21.1	20.7
Ng d = 15–50	299	328	172	1027	1030	718	415	162	1104	15	258
$HAGB_{<111>}$/(LAGB+$HAGB_{<111>}$)	0.036 ± 0.016	0.159 ± 0.071	0.030 ± 0.022	0.012 ± 0.000	0.026 ± 0.006	0.011	0.202 ± 0.093	0.205 ± 0.099	ND[b]	0.193 ± 0.123	ND[c]
Np LAGB+$HAGB_{<111>}$	297,354	395,293	122,626	274,058	678,853	291,616	123,068	24,592	73,269	1954	177,383
Troilite											
$GOS_{d15\text{-}50}$ (°)	1.19 (0.56) ± 0.01	2.75 (1.66) ± 0.13	2.68 (1.81) ± 0.23	4.54 (2.23) ± 0.04	7.36 (3.64) ± 0.66	5.31 (2.84)	4.07 (2.04) ± 0.51	4.03 (1.39) ± 0.72	1.36 (1.26) ± 0.18	1.14 (0.76) ± 0.45	0.955 (0.215) ± 0.052
Mean d d = 15–50 (μm)	23.7	25.6	24.2	21.0	20.7	17.1	23.5	21.9	26.0	22.2	22.6
Ng d = 15–50	562	952	1013	38[d]	52[d]	71[d]	2502	204	1853	191	723

Note: Values in parentheses give means of standard deviations weighted by number of grains (Ng) and are a measure of intrinsic variability; "±" values give the ±1 standard deviation of multiple determinations in different maps and are a measure of repeatability.

[a]PTS = polished thin section; OM = optical microscopy; EBSD = Electron Backscatter Diffraction; CSS = conventional shock stage (with 2 most frequent modes shown); WSS = weighted shock stage; N = number of grains used in shock stage analysis; Ng = number of grains used in EBSD analysis of GOS and Sk; Np = number of pixels with misorientation boundaries (denoised data); d = equivalent grain diameter, the diameter of a circular grain with the same area as the grain; GOS = Grain Orientation Spread, the average intragranular misorientation within grains of a given d range, values show averages of different maps weighted by Ng; Sk = GOS skewness = (mean GOS)/(median GOS), a measure of GOS asymmetry within grains of a given d range, values show averages of different maps weighted by Ng; $R_{2\text{-}10}$ = intragranular disorientation rotation axis parameter in olivine crystal frame (Ruzicka et al., 2024), values show averages of different maps (denoised data) weighted by Np; T_{deform} = model deformation temperature based on $R_{2\text{-}10}$ (Ruzicka et al., 2024), values in square brackets for T_{deform} show averages of estimated accuracy (Ruzicka et al., 2024) weighted by Np; Np 2–10 CRA = the number of pixels with 2°–10° disorientation in a CRA plot; $HAGB_{<111>}$/(LAGB+$HAGB_{<111>}$) is a measure of the relative importance of deformation twinning to subgrain boundary deformation, and corresponds to the number of pixels in bcc metal (denoised data) corresponding to high angle grain boundaries (HAGBs) with 51°–61° misorientation, primarily in <111> twin orientation, relative to the total number of pixels of low angle grain boundaries (LAGBs) with 2°–15° misorientation and HAGB pixels with 51°–61° misorientation. This ratio probably slightly overestimates the twinning proportion because not all the HAGBs have a <111> twin orientation.

[b]Not determined (ND) because most HAGBs are not <111> twins, but rather variably oriented boundaries caused by recrystallization.

[c]Not determined (ND) because most HAGBs in the 51°–61° range are <101> boundaries, not <111> twins.

[d]Low Ng values caused by fine grain size of troilite in aggregates.

19455100, 0, Downloaded from https://onlinelibrary.wiley.com/doi/10.1111/maps.70246 by ALEX RUZICKA , Wiley Online Library on [09/11/2026]. See the Terms and Conditions (https://onlinelibrary.wiley.com/terms-and-conditions) on Wiley Online Library for rules of use; OA articles are governed by the applicable Creative Commons License

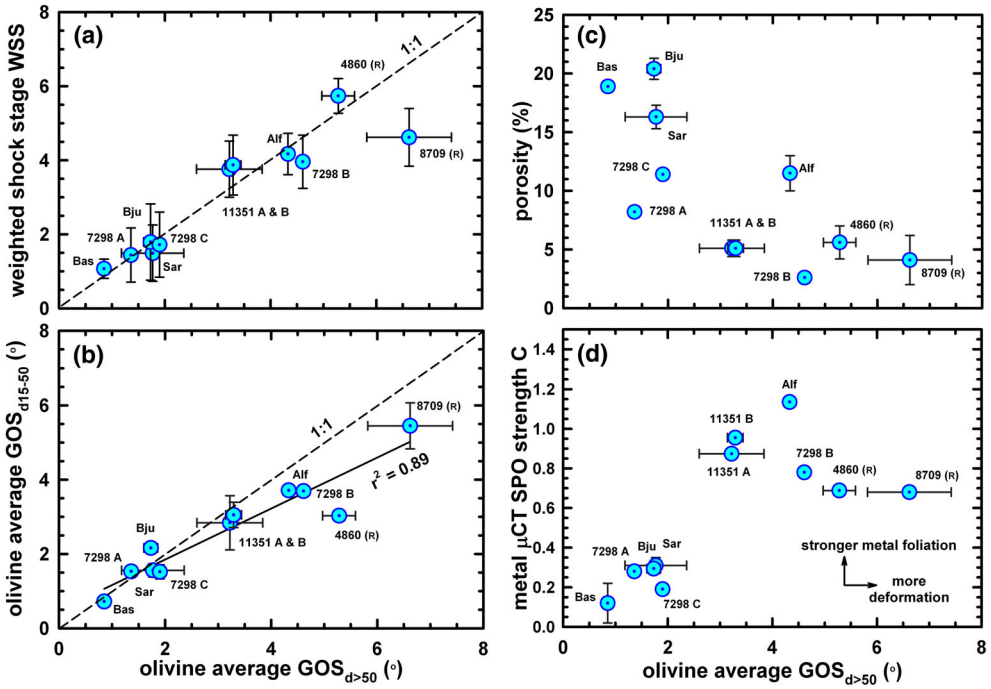


FIGURE 1. Relationship between average grain orientation spread for olivine with equivalent grain diameters d > 50 µm ($GOS_{d>50}$) and other parameters, including (a) weighted shock stage (WSS); (b) average olivine GOS_{d15-50} for d = 15–50 µm grains; (c) porosity; and (d) µCT strength parameter C for metal grains. R = significant olivine recrystallization.

Weakly Shocked Chondrites

Baszkówka contains distinctive features. It has well-known large intergranular voids or vugs that appear between chondrules (e.g., Friedrich, Macke, et al., 2008) and relatively scarce pockets of fine-grained matrix (Figure 2a). Most vugs are irregularly shaped, but some within the matrix are circular (Figure 2a). The irregular voids are sometimes bridged by silicates, including olivine, pyroxene, plagioclase, or chondrule mesostasis (calcic pyroxene and plagioclase) (Figure 2a). In addition, chondrule olivine crystals that are adjacent to the large voids sometimes have well-formed crystal faces (Figure 2b), as has been previously noted (Krzesińska & Almeida, 2019; Wlotzka & Otto, 2001). Matrix pockets contain what appear to be crystal fragments, including shards of troilite (Figure 2a). There is good evidence for localized recrystallization effects in olivine and orthopyroxene that created small, polygonal grains meeting with triple junctions composed of HAGBs (Figure 2b), as well as recovery effects in olivine, troilite, and orthopyroxene to create subgrain boundaries (Figure 2c). Some bcc metal grains have an internal lath texture reminiscent of lath martensite (Figure 2b inset) (Maki, 2012; Mao et al., 2018), whereas other grains have a single, uniform orientation. Other metal grains in Baszkówka reportedly have a plessite texture (Friedrich, Rubin, et al., 2014) composed of intergrowths between Ni-poor and Ni-rich metal, unlike the martensite grains we observed. However, Rubin (2004) noted that annealing of martensite can create plessite.

Saratov has contrasting deformation features for silicates and bcc metal. Silicates have low GOS but are significantly fractured, with fractures often encircling or occurring within chondrules (Figure 2d). Small chondrule fragments are present in the matrix (Figure 2d). Curved subgrain boundaries are present in olivine, orthopyroxene, and clinoenstatite and resemble those in Baszkówka though are less prominent.

In contrast, there are no fractures through metal. The metal has much higher GOS than silicates (on average ~4× higher than olivine; Table 3). Some remarkable coarse (mm-sized) metal grains are present: these are molded around chondrules, penetrate the chondrules somewhat, and fully enclose smaller silicate fragments (Figure 2e,f). This metal appears to have been mobilized in a fluid- or liquid-like state. Silicates surrounding this coarse metal are relatively less fractured than elsewhere. The coarse metal in Figure 2e,f has one dominant orientation and is a single crystal (Figure 2e) but is distorted at its edges where in contact with the surrounding silicates, in some places reaching ~30° misorientation relative to the average grain orientation (Figure 2f). The coarse metal also contains twins that are composed of pairs of mostly ~55°–60° boundaries with

19455100, 0, Downloaded from https://onlinelibrary.wiley.com/doi/10.1111/maps.70246 by ALEX RUZICKA , Wiley Online Library on [09/11/2026]. See the Terms and Conditions (https://onlinelibrary.wiley.com/terms-and-conditions) on Wiley Online Library for rules of use; OA articles are governed by the applicable Creative Commons License

<111> disorientation rotation axes. These twins have non-uniform thickness, pinching in where they intersect other twins or silicate inclusions and pinching out farther away from these features (analogous to sausage links, Figure 3e). Twin lamellae with non-uniform thickness are characteristic of deformation twins (Passchier & Trouw, 2005, p. 37). The twin lamellae are mainly straight but are bent in places, especially at the warped edges of the coarse grains. Lamellae interiors tend to have low GOS values compared to adjacent metal.

Some coarse troilite is present between chondrules, appears to have been fluidized, and is somewhat fractured, though less than silicates.

As in Saratov, fracturing is prevalent in **Bjurböle** silicates. Circumchondrule fractures are obvious in some places (Figure 2g). Similarly, Soini et al. (2023) found that fractures around Bjurböle chondrules (continuous "gaps surrounding chondrules") occur in 3-D μCT datasets. These circumchondrule fractures probably cause the extreme friability of this meteorite (Soini et al., 2023). Small fragments are present in matrix areas. Other areas that include more troilite or metal are less fractured (Figure 2g). Although Bjurböle lacks coarse metal, coarser troilite areas appear to have been mobilized in a fluid-like state. Bjurböle olivine, orthopyroxene, and troilite grains all contain a notable proportion of curved subgrain boundaries that could have been produced by recovery.

Lithologies A and C in NWA 7298 are both weakly shocked lithologies (CSS = S1 and S2, respectively—Table 3), the latter as a large clast and the former as the host of the meteorite. As with Saratov and Björbole, silicates show a dominant fracturing, with a cataclastic texture present for Lithology A (Figure 2h). Fractures are sometimes filled with weathering products. Silicates have low GOS values (e.g., average $GOS_{d>50} \sim 1.4°–1.9°$ for olivine; Table 3). Despite this, minor recrystallized olivine was found in Lithology C.

In contrast to silicates, bcc metal is unfractured, has strong plastic deformation (average $GOS_{d15\text{-}50} \sim 9.4°–11.6°$, the highest among the samples studied—Table 3) and was fluidized (Figure 2h–j). Twins are uncommon in bcc metal from NWA 7298 Lithology A and C. In Figure 2j, two metal grains have GOS values of ~27°–30°, enclose partial twin lamellae, and have more deformation at their edges against silicates. Disorientations from the average orientation of metal grains at crystal edges are related to the type of silicate interface; higher disorientations in metal occur against plagioclase, glass, chondrule mesostasis or grain contacts, and lower disorientations occur adjacent to flat olivine or pyroxene crystals (Figure 2j). This suggests that shock impedance (Ogilvie et al., 2011; Stöffler et al., 1991) contrasts partly controlled the deformation of metal, and thus that the metal was deformed in situ. In Lithology C, recrystallized metal is present locally.

Troilite grains in both lithologies consist of pitted, granular aggregates composed mainly of fine-grained ($d < 5$ μm), weakly deformed (GOS < 1°) grains; coarser grains in the aggregates are more deformed (GOS ~4°–10°) and contain curved subgrain boundaries (Figure 2h). The pits in the aggregates are either plucked grains or original voids; some are filled with weathering products. The troilite aggregates in NWA 7298 resemble those in the Ozerki shocked L6 chondrite that were attributed to recrystallization (Macente et al., 2025), and the same interpretation can be made for troilite in NWA 7298 Lithology A and C.

Strongly Shocked Chondrites

NWA 7298 Lithology B occurs as a clast within Lithology A but has much more deformed silicates. Average olivine $GOS_{d>50}$ is ~4.6° for Lithology B and ~1.4° for Lithology A (Table 3). Melt pockets produced by shock melting are present in Lithology B. Despite more deformed silicates, metal and troilite grains in Lithology B resemble those present in the other two lithologies (A, C) of the meteorite. Troilite consists of granular aggregates reminiscent of those in Lithology A and C but has somewhat coarser grains (~5–10 μm across). The aggregates sometimes form stubby veins between chondrules and appear to have been fluidized. Bcc-metal is highly deformed, apparently fluidized, and has few twins.

Lithologies A and B in NWA 11351 are type 3–4 chondrites that differ drastically in texture. In Lithology A, closely spaced and tight-fitting chondrules are present (cluster chondrite texture), whereas in Lithology B, there is an almost complete lack of chondritic (chondrule matrix) texture (Ruzicka et al., 2024). Lithology A forms a lensoid clast between Lithology C (not studied here) and Lithology B (Ruzicka et al., 2024). Both lithologies were strongly shocked, involving melting of chondrule mesostases and melting or vitrification of olivine and plagioclase to produce a "spotted matrix" in Lithology A (Ruzicka et al., 2024).

Metal and troilite grains in the two NWA 11351 lithologies contain distinctive textures. Bcc-metal grains in both lithologies have good <111> twinning (Figure 3a). The twin lamellae have uneven thickness and in places have a "sausage-link" morphology (Figure 3a) reminiscent of those in Saratov (Figure 2e). Twins sometimes cross-cut one another or occur within other twins (Figure 3a). Most metal grains have two to three sets of twin orientations, with the most prominent commonly angled from upper right to lower left as in Figure 3a and the other sets at high angles to this. Metal grains in both lithologies form vein-like segments in places

19455100, 0, Downloaded from https://onlinelibrary.wiley.com/doi/10.1111/maps.70246 by ALEX RUZICKA , Wiley Online Library on [09/11/2026]. See the Terms and Conditions (https://onlinelibrary.wiley.com/terms-and-conditions) on Wiley Online Library for rules of use; OA articles are governed by the applicable Creative Commons License

and often have silicate inclusions (as in Figure 3a, which has unusually large inclusions) suggestive of metal fluidization. In rare cases, metal grains were recrystallized along their edges or in bands inside the grains.

Lithology A of NWA 11351 contains aggregates up to 6.5 mm long composed mainly of troilite grains (~100 μm across) and many silicate inclusions (Figure 3b,c). In some places, the silicate inclusions in the aggregates resemble silicates outside the aggregates (inset 'a' in Figure 3b); in other places, they are aligned (inset 'b' in Figure 3b). Inclusions within troilite include grains with compositions like olivine (by far most common), feldspar, or pyroxene, but many of the silicates do not index and appear to be amorphous. Figure 3b shows an ~3-mm-long aggregate, which embays or partly encircles chondrules. The troilite must have been fluidized to incorporate so many silicate inclusions and to flow around chondrules (Figure 3b). Troilite appears to have been injected into the interior of a prominently embayed chondrule (Figure 3c, circled area).

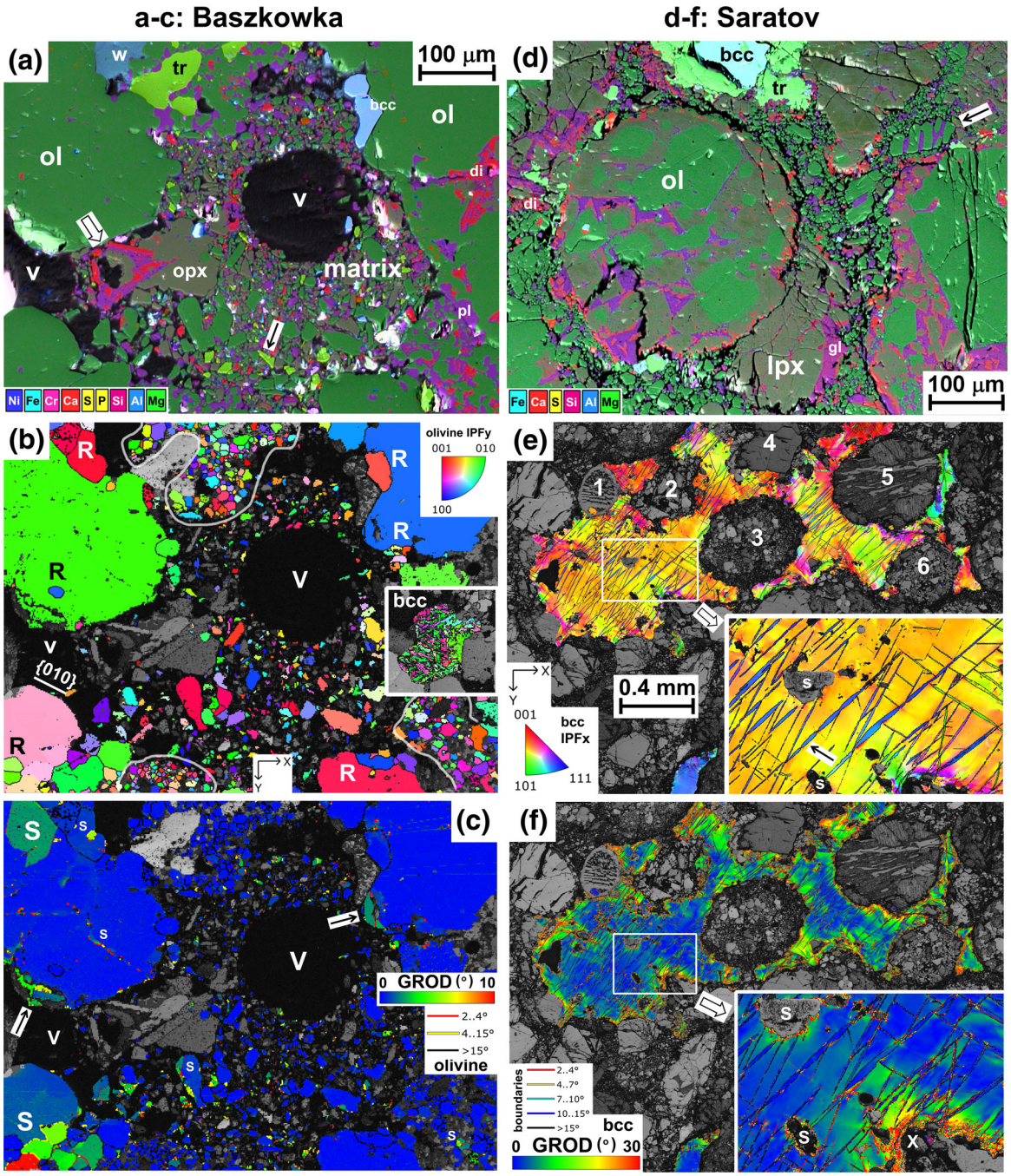
Troilite grains in NWA 11351 Lithology A and B are significantly deformed (average $GOS_{d15\text{-}50} \sim 4.1°–5.3°$, Table 3) and partly recrystallized (Figure 3c). Recrystallized domains (GOS < 1°) form bands or chains of granular grains (mostly <50 μm across) that cross-cut or occur adjacent to larger deformed grains (Figure 3c). Troilite grains also contain twin lamellae of non-uniform thickness and reduced GOS values that have specific angular misorientations (mostly ~87° ± 4°) and disorientation rotation axes (<−1–120>).

In **Alfianello**, strong shock deformation largely transformed feldspar into maskelynite, which has a smooth, unfractured appearance (Figure 3d) and which is amorphous (Figure 3e). Bcc-metal and troilite grains were largely recrystallized (Figure 3d). Some metal areas consist of plessite (Figure 3d,e), an intergrowth of low-Ni and high-Ni metal phases (e.g., Bennett & McSween, 1996; Luo et al., 2024), which in Alfianello index as bcc phase and tetrataenite, respectively. Metal is unfractured, but troilite grains contain some fractures, and silicates (olivine, calcic pyroxene, and low-Ca pyroxene) contain many fractures (Figure 3d). Melt pockets and veins are present.

In the "blackened" melt breccia **NWA 8709**, chondrules and clasts are present in a fine-grained, largely crystalline igneous matrix ("melt matrix") produced by shock melting (Ruzicka et al., 2020; Figure 3f,g). A

FIGURE 2. SEM and EBSD images of weakly shocked lithologies. (a) Electron + EDS image centered on matrix and adjacent grains in Baszkówka (map TM9). Features include irregular and circular voids (v, black), olivine (ol, green), troilite (tr, yellow-green) including triangular shard in matrix (thin arrow bottom center), bcc metal (bcc, light blue), orthopyroxene (opx, tan), diopsidic pyroxene (di, red), plagioclase (pl, purple), minor weathering product (w, darker blue), bridging crystals of di + pl across voids that are similar to chondrule mesostasis (fat arrow at left). (b) Same area as in part (a) but showing BC + olivine IPFy. Features include recrystallized olivine grains (R) and pockets of small, recrystallized grains (outlined); and a well-preserved {010} face of olivine adjacent to a void. The inset shows a BC + IPFz image (excerpt from map TM4) of a bcc metal grain ~100 μm across that has lath martensite texture; see part (e) for bcc color legend. (c) Same area as in part (a) but showing BC + GROD angle and subgrain boundaries (S) for olivine. Most subgrain boundaries occur within the interiors of olivine grains and do not appear to be sample preparation artifacts; possible exceptions are shown by arrows where subgrains occur on the edges of voids. (d) Electron + EDS image of Saratov (map TM7), same abbreviations and colors as in part (a) but also including glass or devitrified glass (gl, purple). Features include fractures within and around chondrules, a small fragment of barred olivine chondrule (arrow upper right), and cataclastic texture in matrix areas. (e) Coarse metal and adjacent area in Saratov (excerpt from map DM1), BC + IPFx for bcc metal. The coarse metal is a single grain that envelopes silicates and chondrules (1, 2, 3, 4, 5, 6) and has changes in crystal orientation at contacts with silicates. The insert is an enlargement to better show prominent twin lamellae, which have thinner and thicker portions forming a "sausage-link" morphology (arrow). Some silicate inclusions (s) are fully embedded in the metal. (f) Same area as in part (e) but showing BC + GROD angle and subgrain boundaries for bcc metal; the inset shows an enlargement. At metal–silicate contacts the metal has higher GROD angles and more subgrain boundaries (mostly 2°–4° misorientations) indicative of more deformation, such as at X in the enlargement. (g) Electron + EDS image of Bjurböle (excerpt from map DM1), same abbreviations and colors as in part (a) but also including phosphate (ph, orange) and low-Ca pyroxene (lpx, tan-olive) that is a combination of orthopyroxene and clinoenstatite. Features include prominent circum-chondrule fractures, and less silicate fracturing in areas with more troilite or bcc metal. (h) Area centered on troilite aggregate in NWA 7298 Lithology A (map TM12), BC + GROD angle for troilite. Inside the aggregate, some larger grains (1, 2) have higher GROD angles and subgrain boundaries, whereas many smaller grains have uniform low GROD angle and appear to be recrystallized (R). There are pores (p) both within and outside the aggregate, some filled with weathering products (w). The area surrounding the troilite has a cataclastic texture. (i) Area centered on a bcc metal grain in NWA 7298 Lithology A (map TM8), BC + phases (ol = olivine, green; lpx = low-Ca pyroxene, orange; pl = plagioclase, purple; di = diopsidic pyroxene, red; bcc = bcc metal, light blue; tr = troilite, yellow; chr = chromite, dark blue; ph = phosphate, turquoise). Features include bcc enveloping silicates, including two barred olivine chondrule fragments (bo1, bo2), and a cataclastic texture of silicates including a triangular shard of clinoenstatite (arrow top). Black areas are mainly pores or cracks; metal is unfractured. (j) Same area as in part (i) but showing BC + GROD angle for all indexed phases. The two larger bcc metal grains are highly deformed in contrast to all other phases and have few twins (high angle grain boundaries with ~50°–60° misorientation and <111> rotation axis). The metal grains are warped at their edges (elevated GROD angle) in contact with silicates, especially adjacent to feldspar or feldspathic glass (arrows) or grain boundaries.

19455100, 0, Downloaded from https://onlinelibrary.wiley.com/doi/10.1111/maps.70246 by ALEX RUZICKA , Wiley Online Library on [09/11/2026]. See the Terms and Conditions (https://onlinelibrary.wiley.com/terms-and-conditions) on Wiley Online Library for rules of use; OA articles are governed by the applicable Creative Commons License



textural continuum occurs between larger objects down to matrix.

Larger objects include "chondrules" and "clasts", up to ~2.5 mm and down to ~50 µm across (Figure 3f). They contain deformed olivine and pyroxene but also contain recrystallized olivine (and rarely low-Ca pyroxene) domains with GOS values <1° (e.g., "R" in chondrules/clasts 1 and 4 in Figure 3f). These recrystallized domains in olivine are more conspicuous, prevalent, and coarser than in other chondrites discussed above (e.g., compare Figure 3f NWA 8709 to Figure 2b Baszkówka).

Finer grained materials include "matrix", polyphase regions dominated by ~1–5 µm-diameter grains, and "clumps" (~10–50 µm across) composed of similar-sized grains but consisting mainly of (~98%) olivine (Figure 3f, g). The matrix consists of a granular assemblage of fine-grained pigeonite, olivine, troilite, and globules of metal and troilite, with troilite often on the periphery of metal

19455100, 0, Downloaded from https://onlinelibrary.wiley.com/doi/10.1111/maps.70246 by ALEX RUZICKA , Wiley Online Library on [09/11/2026]. See the Terms and Conditions (https://onlinelibrary.wiley.com/terms-and-conditions) on Wiley Online Library for rules of use; OA articles are governed by the applicable Creative Commons License

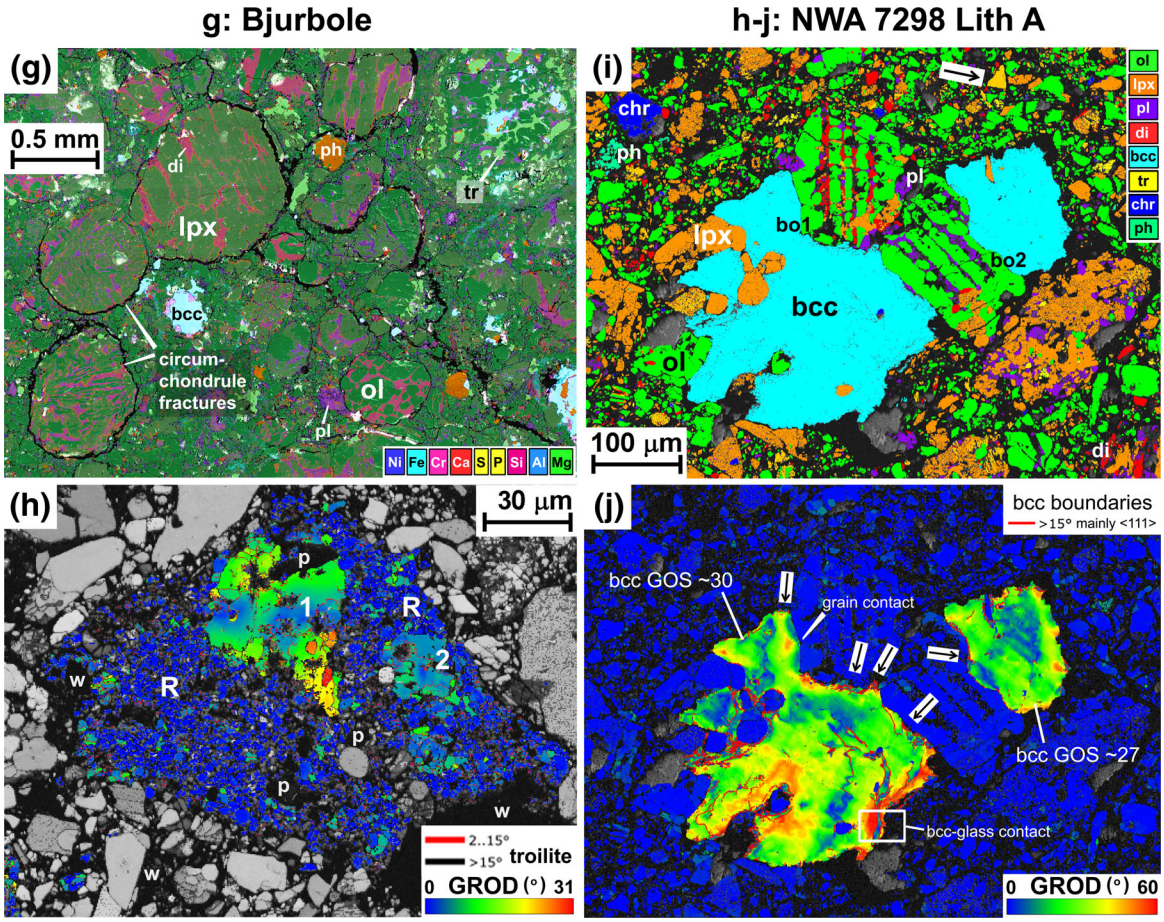


FIGURE 2. Continued

(Figure 3g). Silicates have low GOS values (<1°), and metal shows a lath martensite texture (although much metal has been weathered). Although rich in olivine, clumps also have other phases such as glass, chromite, troilite, bcc metal, and pigeonite interstitial to olivine. Some clumps are surrounded by coronas rich in pigeonite grains radially directed away from the clumps, but most clumps lack coronas (Figure 3g). Larger olivine crystals in the clumps have higher GOS values with subgrain boundaries and other internal misorientations, and these grade into smaller grains with lower GOS and high angle boundaries, reminiscent of the troilite aggregates in NWA 7298.

The edges of recrystallized domains in chondrules sometimes grade into fine-grained olivine borders that resemble clumps (outlines of chondrules/clasts 2 and 4 in Figure 3f). These borders themselves grade into matrix.

The most notable features of the "blackened" melt breccia **NWA 4860** are a high shock stage corresponding to extensive olivine recrystallization, the presence of vugs into which metal and troilite have grown, and a uniformity in crystal lattice orientation of troilite.

NWA 4860 is a true S6 chondrite, with the S6 designation based only on olivine and not on other features such as melting or local presence of high-pressure phases. With optical microscopy, roughly 75% of the olivine grains examined have evidence for recrystallization (any grain with such evidence was counted as S6), leading to the highest WSS value we have determined for a chondrite to date (~5.7) and a CSS value of 6 (Table 3). EBSD data for olivine show obvious recrystallized domains among deformed grains (Figure 3h). For olivine of all grain sizes, the large area map (LAM) has a bimodal GOS distribution, with GOS $\leq 1°$ corresponding to recrystallized grains, and GOS ~1°–16° corresponding to more deformed grains (Figure 3h). Considering the recrystallized and deformed grains separately in the LAM, there are 19,362 recrystallized grains with average (±SD) GOS $\sim 0.29° \pm 0.15°$, and 21,798 deformed grains with average GOS $\sim 4.0° \pm 2.0°$. The recrystallized fraction of olivine is therefore ~47% by number of grains.

NWA 4860 contains irregular vugs ~10–450 µm across (Figure 3i). There are also two elongate vugs that are up to ~1.7 mm long whose long axes are oriented

19455100, 0, Downloaded from https://onlinelibrary.wiley.com/doi/10.1111/maps.70246 by ALEX RUZICKA , Wiley Online Library on [09/11/2026]. See the Terms and Conditions (https://onlinelibrary.wiley.com/terms-and-conditions) on Wiley Online Library for rules of use; OA articles are governed by the applicable Creative Commons License

roughly parallel to a visual lineation defined by metal and silicates (Figure 3j). Bcc-metal and troilite grains project into some of the vugs and appear to have grown into them (Figure 3i). In one place, metal with lath martensite texture (characteristic of this meteorite) has grown into a vug from a base portion that is intergrown with silicates; in turn, a single crystal of subhedral troilite (~150 μm across) has grown atop the metal inside the vug (Figure 3i). For this troilite crystal, the facets of the troilite within the vug appear to correspond to {01-10} "prismatic" planes, the pole to the (0001) basal plane points close to the Z-direction normal to the section, and the <−12-10> direction in troilite points close to the left–right X-direction (IPFx green coloration, Figure 3i). Elsewhere in smaller vugs, silicates including olivine, orthopyroxene, diopsidic pyroxene, and plagioclase partly bridge the vugs (Figure 3i).

Most troilite grains in the section of NWA 4860 that was studied have similar crystal orientations, with the pole to (0001) lying close to the Z direction (IPFz red coloration in Figure 3k). This is the same orientation as for the subhedral vug crystal in Figure 3i. Orientation domains differ somewhat across ~2–4 mm scales. The troilite in NWA 4860 appears to be disconnected in the plane of the section (Figure 3j,k), but it could be connected in the third dimension to form a large interstitial network. Besides uniform crystal orientation, NWA 4860 has the lowest average $GOS_{d15\text{-}50}$ for troilite of any lithology (0.96° ± 0.05°, Table 3).

Other features of NWA 4860 include: (1) igneous textures in a fine-grained matrix that is rich in pigeonite and that contains some metal–troilite globules; (2) plagioclase that is present mostly inside chondrule mesostases or in veinlets that cross-cut olivine; and (3) the presence of recrystallization textures in orthopyroxene that are like olivine in coarseness and almost as prevalent. These features are also found in NWA 8709, except that there is much more recrystallized pyroxene in NWA 4860.

Plastic Deformation in Different Minerals

Little work has been done to evaluate how GOS values compare for different minerals. For this study, the most useful comparisons in the acquired data sets are made for grains in the d = 15–50 μm diameter range, because this size range is always well-populated with grains in LAM and DM maps at the steps sizes used (2.5–4.6 μm for LAMs, 0.28–2.5 μm for DMs; Table S1).

Figure 4 shows GOS data for olivine, bcc metal, and troilite. In Figure 4a, $GOS_{d15\text{-}50}$ values are compared for different lithologies. $GOS_{d15\text{-}50}$ values for metal and troilite tend to be higher than olivine for all but the most strongly shocked lithologies (Alfianello, NWA 8709, NWA 4860). With these exceptions, *$GOS_{d15\text{-}50}$ values increase in the sequence olivine < troilite < bcc metal* (Figure 4a). For the exceptions, metal and troilite were recrystallized or partly to wholly melted ("r" and "m" labels, respectively, in Figure 4).

In Figure 4b, the ratio of $GOS_{d15\text{-}50}$ values for bcc metal and troilite to that in olivine are plotted on the ordinate and olivine $GOS_{d>50}$ is plotted on the abscissa. This plot shows an inverse relationship between deformation intensity as given by olivine $GOS_{d>50}$ and the $GOS_{d15\text{-}50}$ ratios for metal/olivine and troilite/olivine. In the weakest shocked lithologies (olivine $GOS_{d>50}$ <2°), average $GOS_{d15\text{-}50}$ values for metal/olivine and troilite/olivine range from ~2.7 to 7.6 and ~1.2–4.8, respectively (Figure 4b).

Bcc-metal grains in the chondrites have textures indicative of deformation twinning (Sec. 3.2), raising the question of how important this was for plastic deformation in metal and whether it relates to shock intensity. There are significant differences between the lithologies in the amount of metal that is twinned. The prevalence of twinning can be quantified by counting all pixels associated with high angle (51°–61°) grain boundaries (HAGBs) dominated by <111> disorientation rotation axes and associated with twins (a parameter we designate as $HAGB_{<111>}$) and the number of pixels associated with low angle (2°–15°) grain boundaries or subgrain boundaries that contribute to GOS (the parameter LAGB). The ratio $(HAGB_{<111>})/(LAGB+HAGB_{<111>})$ (Table 3) is therefore related to the fraction of disorientations caused by twinning compared to the total amount of disorientations corresponding to $HAGB_{<111>}$ and LAGB. We refer to this metric as a "twinning proportion". This is not a measure of the amount of strain, rather a count of pixels associated with twinning or with low angle boundaries.

Figure 5 shows the twinning proportion in bcc metal compared to deformation intensity as given by olivine $GOS_{d>50}$. In most lithologies, the twinning proportion is low (<0.04), whereas in Saratov, NWA 11351, and NWA 8709, it rises to ~0.15–0.20 (Figure 5). This suggests that *most of the disorientations by number in metal are related not to twinning but rather to low angle misorientations*. Moreover, Figure 5 shows that low twinning proportions occur in both weakly shocked (Baskówka, NWA 7298 Lithology A & C, Bjurböle) and more strongly shocked lithologies (NWA 7298 Lithology B); and high twinning proportions occur in both weakly shocked meteorites (Saratov) and more strongly shocked lithologies (NWA 11351, NWA 8709). This implies that *twinning in bcc metal was not primarily related to overall shock intensity as recorded in olivine*. A somewhat different conclusion was reached by Luo et al. (2024), who found that the bcc metal twins (which they called Neumann Bands) were

19455100, 0, Downloaded from https://onlinelibrary.wiley.com/doi/10.1111/maps.70246 by ALEX RUZICKA , Wiley Online Library on [09/11/2026]. See the Terms and Conditions (https://onlinelibrary.wiley.com/terms-and-conditions) on Wiley Online Library for rules of use; OA articles are governed by the applicable Creative Commons License

characteristic of weakly shocked (S1-S2) chondrites, although they were found in S4-S5 chondrites as well. As <111> twins in bcc grains are thought to form by shear (Lagerlöf, 1993; Zhang et al., 2016) and to be promoted by lower temperatures and in larger grains (Zhang et al., 2016), we speculate that <111> twinning in Saratov, NWA 11315, and NWA 8709 were enhanced by some combination of having higher shear stress, higher strain rates, lower temperature, and larger grains.

GOS Skewness and Grain Size for Olivine

GOS skewness (Sk = mean GOS/median GOS) is a measure of the asymmetry or skew of GOS distributions for a population of grains (Ruzicka et al., 2024; Ruzicka & Hugo, 2018). It is a type of dispersion sensitive to the number and GOS values of grains in the "tails" of a GOS distribution (almost always the high-GOS tail because GOS distributions in shocked rocks typically have positive skew). It has been used to identify post-deformation annealing or recovery (Ruzicka & Hugo, 2018), most reliably by considering how Sk varies with grain size (Ruzicka et al., 2024).

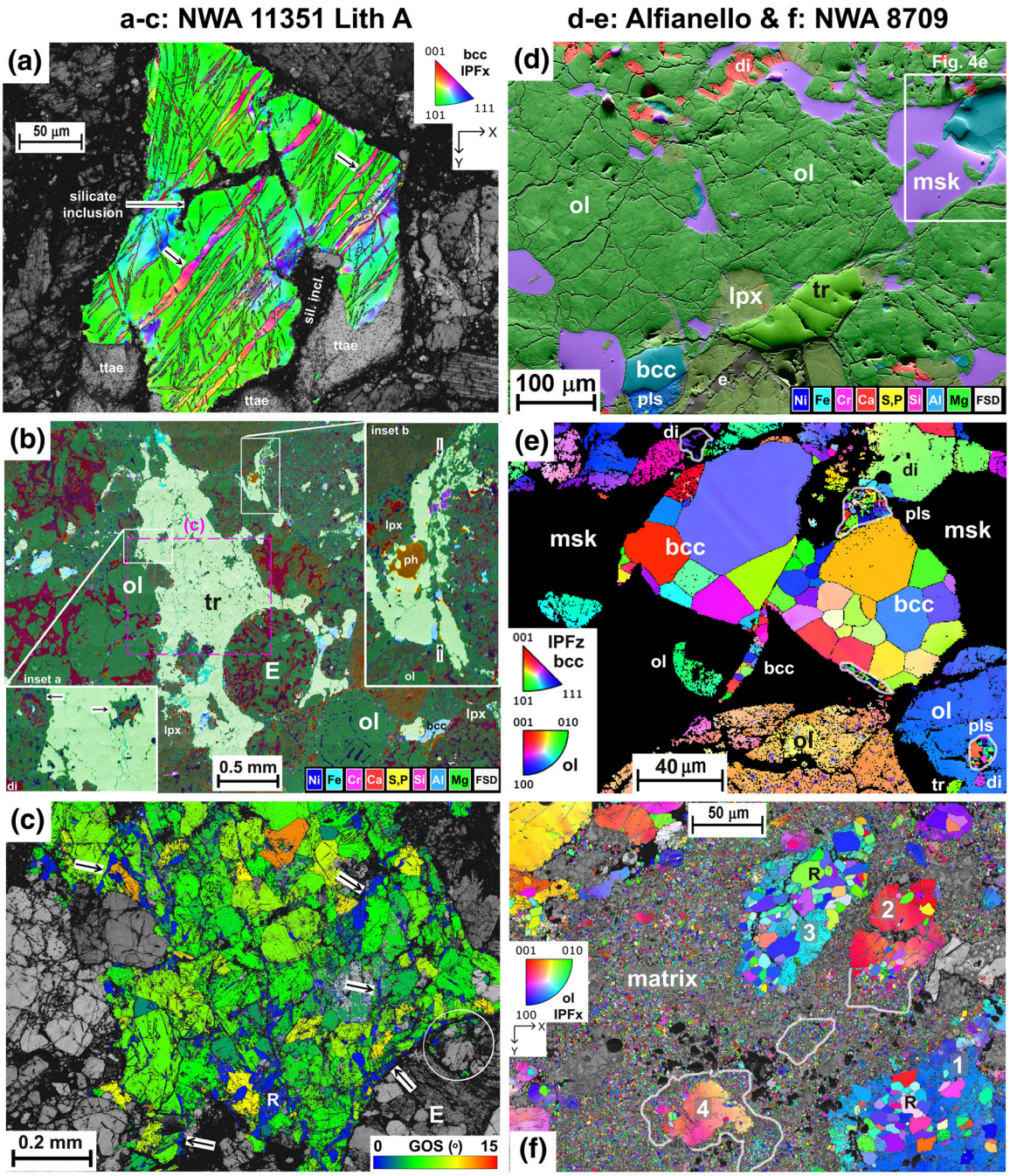
Table 3 gives Sk-d data for olivine, and Figure 6 plots the results. Different patterns are seen. Olivine in Alfianello and the genomict breccias NWA 7298 and NWA 11351 have Sk values that increase somewhat as grain size decreases (Figure 6a), whereas olivine in the melt breccias NWA 8709 and NWA 4860 have Sk values that increase dramatically (factor of ~2–3) for d values <15 μm (Figure 6b). In olivine from Bjurböle, Sk decreases with grain size except for the smallest grain sizes (d < 5 μm), at which point Sk increases (Figure 6c). Baszkówka and Saratov olivine have almost uniform Sk values across different grain sizes except for the smallest grain sizes (d < 5 μm), at which point Sk decreases significantly (Figure 6c).

Olivine Deformation Intensity and Slip

$R_{2\text{-}10}$ is an EBSD deformation parameter for olivine based on intragranular misorientation rotation axis directions for 2°–10° disorientations and is related to the slip system that was activated, with lower values corresponding to more **c**-slip and higher values to more **a**-slip (Hugo et al., 2020; Ruzicka et al., 2024; Ruzicka &

FIGURE 3. SEM and EBSD images of strongly shocked lithologies. (a) Area centered on a single bcc metal grain in NWA 11351 Lithology A (map TM9) showing BC + IPFx for bcc metal. Features include prominent twins in metal (<111> rotation angles, ~50°–60° misorientations) with uneven thickness (arrows) that form a predominant twin set (upper right–lower left), and silicate inclusions enclosed by bcc and by tetrataenite (ttae). (b) Area centered on large coarse troilite aggregate in NWA 11351 Lithology A (excerpt from map DM1), FSD + EDS image. Phase abbreviations and colors are as in Figure 2d; E = prominent embayed chondrule. Inset "a" shows an enlargement illustrating similar textures for silicates in inclusions within the aggregate and outside the aggregate (arrows); inset "b" shows a string of olivine-like inclusions (arrows) within troilite around the edge of a chondrule at right. (c) Portion of troilite aggregate (location shown in part b), BC + GOS for troilite. Troilite grains in the aggregate have variable GOS, including recrystallized grains (r) that often form in bands around or through other troilite grains (arrows). Some troilite appears to have been emplaced inside the embayed chondrule (circle lower right) which otherwise mostly lacks troilite. (d) Typical textures in Alfianello (map TM6), FSD + EDS image. Phase abbreviations and colors as in Figure 2d except msk = maskelynite (purple), pls = plessite, and e = epoxy in a crack. There are many fractures in silicates except for completely unfractured maskelynite, some fractures in troilite, and no fractures in bcc metal or plessite. (e) Closer view in the upper right corner of part (d) centered on bcc metal (map TM8), showing BC + IPFz for all grains, here dominated by olivine, bcc metal, and plessite (abbreviations as in part 2d and 3d). Circled areas highlight plessite and a small diopside grain at top. Maskelynite appears black because it is not crystalline and has almost no BC signal. (f) Small chondrules/clasts (1, 2, 3, 4) set in largely crystalline melt matrix in NWA 8709 (excerpt of map DM1), BC + IPFx for olivine. R = recrystallized grains in olivine; outlined areas indicate areas of olivine-rich clumps within matrix or surrounding chondrules/clasts. (g) Close-up of melt matrix and olivine-rich clumps (1, 2, 3, 4) in NWA 8709 (map TM13), BC + phases image, phase abbreviations same as in Figure 2i, except pig = pigeonite (light orange). A metal–troilite globule is at upper right. Arrows point to lamellae within pigeonite of orthopyroxene (left) or diopside (lower right). (h) BC + olivine GOS image (excerpt from DM1) of NWA 4860 showing recrystallized grains (R) and deformed grains (D). The inset shows the GOS distribution for the large area map (LAM) which has two modes corresponding to recrystallized (GOS ≤1°) and deformed (GOS >1°) grains. (i) Main image is BC + phase for NWA 4860 (map TM5), phase colors and abbreviations are the same as in Figure 2i except tta = tetrataenite (dark blue) and pig = pigeonite (mauve). Irregular black areas are voids (v) into which bcc metal, troilite, or silicates project, or which are crossed by bridging silicates (arrow at right). The white box outlines an area shown in the inset at lower right, which is a BC + IPFx image for bcc metal and troilite. Metal has lath martensite texture and the troilite is a single crystal, with a unit cell orientation as shown schematically. (j) BC + phase image of NWA 4860 (excerpt of map TM1) showing bcc metal and troilite grains together with an apparent lineation direction defined by silicates, metal, and troilite. (k) Same area as in part (j) but showing BC + IPFz for bcc metal and troilite. Troilite grains have predominantly one crystal orientation with <0001> subparallel to Z (red color); the large metal grain has lath martensite texture and appears to have formed as a single grain initially as the orientation patterns are consistent throughout.

19455100, 0, Downloaded from https://onlinelibrary.wiley.com/doi/10.1111/maps.70246 by ALEX RUZICKA , Wiley Online Library on [09/11/2026]. See the Terms and Conditions (https://onlinelibrary.wiley.com/terms-and-conditions) on Wiley Online Library for rules of use; OA articles are governed by the applicable Creative Commons License



Hugo, 2018). Figure 7 shows an almost bimodal distribution in olivine $R_{2\text{-}10}$ and $GOS_{d>50}$ for different lithologies. Weakly shocked lithologies (Baszkówka, Saratov, Bjurböle, NWA 7298 Lith A, NWA 7298 Lith C) with low $GOS_{d>50}$ have higher values of $R_{2\text{-}10}$, and most highly shocked lithologies (NWA 11351 Lith A, NWA 11351 Lith B, Alfianello, NWA 4860, NWA 8709) with high $GOS_{d>50}$ have lower values of $R_{2\text{-}10}$. However, the relationship between GOS and $R_{2\text{-}10}$ is not totally bimodal, because highly shocked lithology B in NWA 7298 also has an elevated $R_{2\text{-}10}$ value, the highest in this study (Figure 7).

DISCUSSION

Deformation Temperature

The EBSD olivine misorientation parameter $R_{2\text{-}10}$ is related mainly to deformation temperature, which could reflect ambient temperature at the time of deformation or

19455100, 0, Downloaded from https://onlinelibrary.wiley.com/doi/10.1111/maps.70246 by ALEX RUZICKA , Wiley Online Library on [09/11/2026]. See the Terms and Conditions (https://onlinelibrary.wiley.com/terms-and-conditions) on Wiley Online Library for rules of use; OA articles are governed by the applicable Creative Commons License

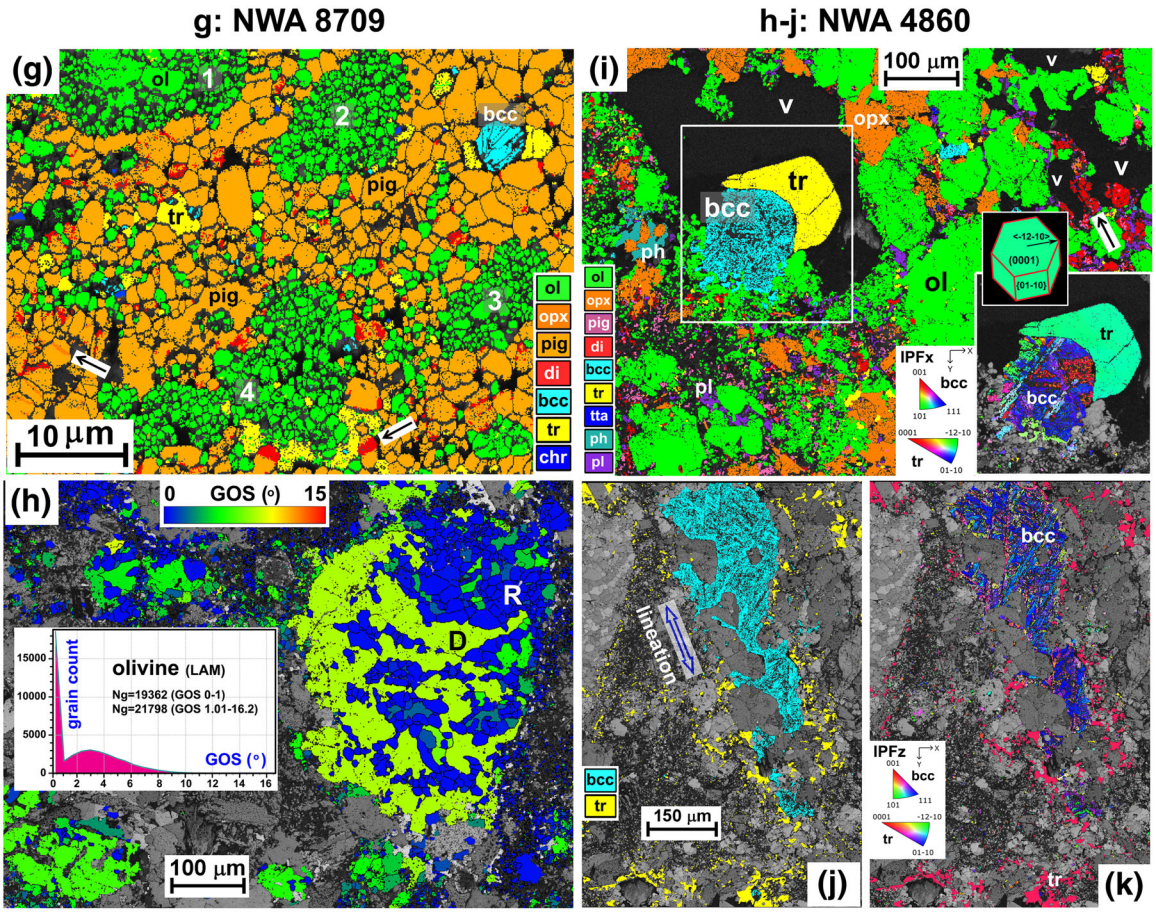


FIGURE 3. Continued

a shock reheating temperature (Hugo et al., 2020; Ruzicka et al., 2024; Ruzicka & Hugo, 2018). It can be used to derive a model deformation temperature, T_{deform} (Ruzicka et al., 2024) (Table 3). Figure 7 shows a mostly inverse relationship between olivine $R_{2\text{-}10}$ and GOS with one prominent exception (NWA 7298 Lithology B). This implies higher deformation temperatures for the weakly shocked chondrites and highly shocked NWA 7298 Lithology B, and lower deformation temperatures for other highly shocked chondrites.

Elevated deformation temperatures were also found for weakly shocked type 3 chondrites and attributed to the widespread accretion of warm chondrules, whereas stronger shocks (CSS ≥ S3–S4) were found to be sufficient to reset $R_{2\text{-}10}$ values (Ruzicka et al., 2024). Thus, for weakly shocked chondrites (Baszkówka, Saratov, Bjurböle, and Lithologies A and C for NWA 7298), elevated $R_{2\text{-}10}$ could in principle be attributed to warm accretion or to weak shocks occurring while the parent bodies were warm, or both. We will return to this question below when discussing data for individual meteorites as well as in the section titled "Warm Chondrule Accretion or Impacts on Warm Bodies?"

Deformation Effects

Table 4 summarizes evidence for deformation styles, recovery, recrystallization, and shock-melting processes ordered by weighted shock stage. All parameters show systematic variation with respect to shock stage indicating that features depend on the overall shock metamorphism intensity.

Deformation Effects in Weakly Shocked Chondrites

In weakly shocked chondrites (WSS ~1.1–1.8), silicate fracturing was a predominant process even while bcc metal and some troilite were being fluidized, as exemplified by Baszkówka, Saratov, Bjurböle, and NWA 7298 Lithology A (Table 4). *This suggests a dominance of brittle deformation for silicates and a more plastic deformation for metal and troilite, in accordance with differences in GOS values.*

19455100, 0, Downloaded from https://onlinelibrary.wiley.com/doi/10.1111/maps.70246 by ALEX RUZICKA , Wiley Online Library on [09/11/2026]. See the Terms and Conditions (https://onlinelibrary.wiley.com/terms-and-conditions) on Wiley Online Library for rules of use; OA articles are governed by the applicable Creative Commons License

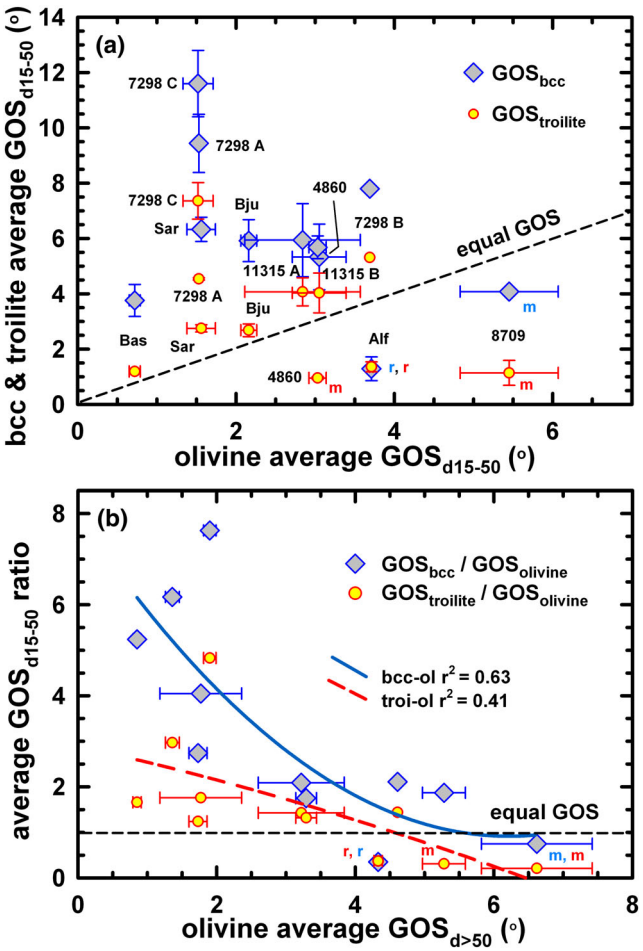


FIGURE 4. Intermineral GOS comparison. Datapoints labeled r and m signify recrystallization or partial-complete melting, respectively, for troilite and metal. (a) Average GOS_{d15-50} values for olivine compared to bcc metal and troilite. Labels: Bas = Baszkówka; Sar = Saratov; Bju = Bjurböle; 7298 A, 7298 B, 7298 C = NWA 7298 Lithology A, B, C respectively; 11,315 A, 11351 B = NWA 11351 Lithology A and B, respectively; Alf = Alfianello; 8709 = NWA 8709; 4860 = NWA 4860. (b) Average GOS_{d15-50} ratio for metal/olivine and troilite/olivine compared to average $GOS_{d>50}$ for olivine. Curves show nonlinear regressions.

None of the weakly shocked chondrites show any evidence for shock melting, but localized recrystallization was found for olivine and orthopyroxene in Baszkówka, for olivine in Bjurböle, and for metal in NWA 7298 Lithology A and C, and recrystallization of troilite was extensive for troilite to create fine-grained aggregates in NWA 7298 Lithology A and C (Table 4). Given the low shock intensity, *minor recrystallization in silicates for Baszkówka and Bjurböle and for metal in NWA 7298 Lithology A and C is best attributed to a static recrystallization process caused by elevated temperatures after shock*.

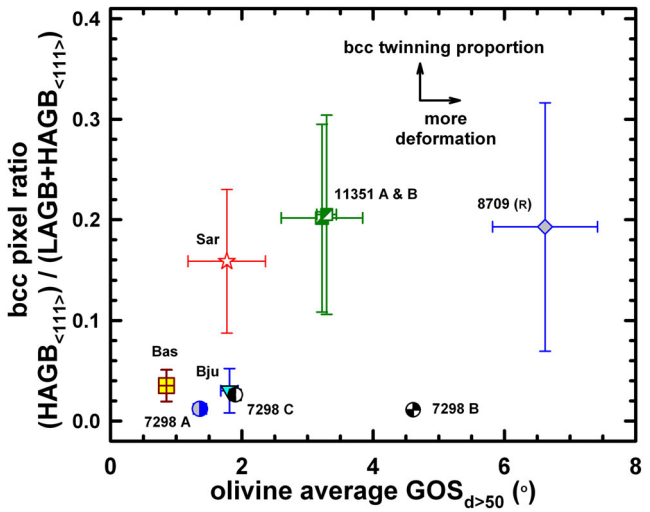


FIGURE 5. Relationship between twinning proportion in bcc metal and $GOS_{d>50}$ in olivine. Twinning proportion is defined by $HAGB_{<111>}/(LAGB+HAGB_{<111>})$, where $HAGB_{<111>}$ is the number of pixels in twin boundaries (56° ± 5° misorientation and mostly <111> rotation axes), and LAGB is the total number of pixels in low angle grain boundaries with 2°–15° misorientation. Meteorite labels as in Figure 4. R = significant olivine recrystallization.

Schmitt (2000) experimentally studied impact deformation of silicates, troilite and metal in a chondritic sample under both ambient (20 °C) and warm (643 °C) conditions and found that one main difference was enhanced recrystallization of troilite in the warm case. For the warm conditions, troilite recrystallization occurred even in the lowest pressure shock experiments (10 GPa), which is compatible with the S1–S2 shock stage of NWA 7298 Lithology A and C, especially considering uncertainties caused by differences in experimental and natural conditions (Sharp & DeCarli, 2006). Thus, *extensive recrystallization of troilite in NWA 7298 Lithology A and C is best attributed to elevated pre-shock temperatures*.

In the weakly shocked chondrites, evidence for recovery in the form of curved subgrain boundaries in grains with minor deformation was found locally for olivine, troilite, orthopyroxene, clinoenstatite, and bcc metal, with more widespread evidence for recovery in Bjurböle (Table 4). These data are compatible with elevated heat following deformation for the weakly shocked chondrites. However, except for Bjurböle, the recovery effects are limited, so the amount of post-deformation heating was limited.

More information about recovery can be obtained from olivine GOS skewness-grain size data. The inferred signature for post-deformation annealing is a decrease in Sk as equivalent grain diameter d becomes smaller, that is,

19455100, 0, Downloaded from https://onlinelibrary.wiley.com/doi/10.1111/maps.70246 by ALEX RUZICKA , Wiley Online Library on [09/11/2026]. See the Terms and Conditions (https://onlinelibrary.wiley.com/terms-and-conditions) on Wiley Online Library for rules of use; OA articles are governed by the applicable Creative Commons License

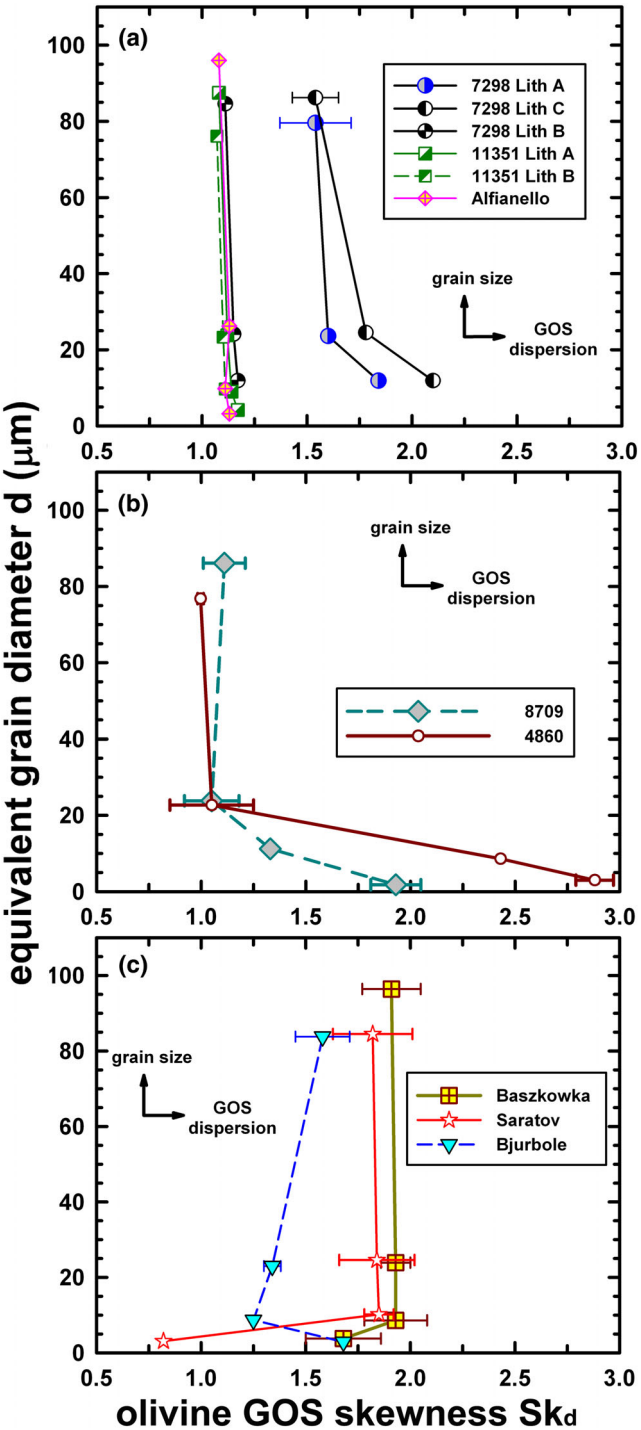


FIGURE 6. Variation in olivine GOS skewness (Sk = [mean GOS]/[median GOS]) with respect to equivalent grain diameter 'd'. Lithologies show different Sk-d patterns. (a) Lithologies that show slight to moderate increases in Sk value as grain size decreases include NWA 7298 Lithology A, B, C; NWA 11351 Lithology A and B; and Alfianello. (b) Lithologies that show large increases in Sk as grain size decreases include NWA 8709 and NWA 4860. (c) Three lithologies show other Sk-d patterns, including a large decrease in Sk for the smallest grains (Baszkówka, Saratov) or a decrease in Sk value followed by an increase in Sk value as grain size decreases (Bjurböle).

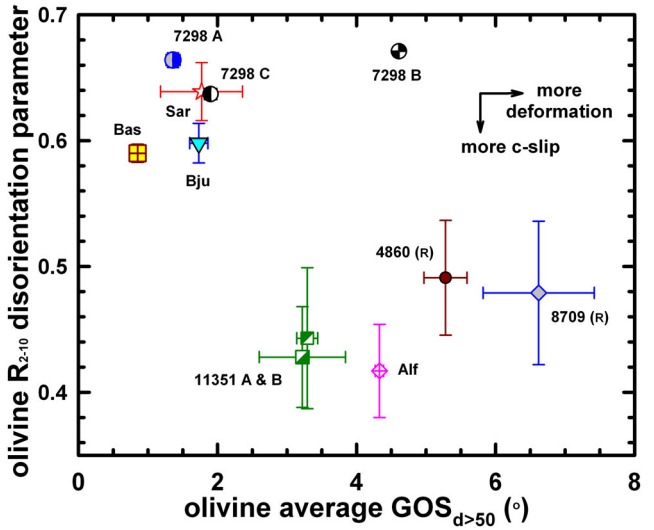


FIGURE 7. Olivine $R_{2\text{-}10}$ versus average $GOS_{d>50}$ for different lithologies. $R_{2\text{-}10}$ is determined by the directions of intragranular disorientation rotation axes in an olivine crystal frame. Meteorite labels as in Figure 4. R = significant olivine recrystallization.

less GOS dispersion with fewer high-GOS grains as grains become smaller (Ruzicka et al., 2024). The only meteorites that fit the Sk-d pattern expected for post-deformation recovery and annealing are Bjurböle, but only for olivine grains with effective d > 5 μm, and Baszkówka and Saratov, but only for olivine grains with effective d < 5 μm (Figure 6). *This implies recovery only on a small scale (≤5 μm) for Baszkówka and Saratov, consistent with limited annealing after shock.*

More extensive annealing on a > 5 μm scale is suggested for Bjurböle but cannot explain the data for smaller grains (d ≤ 5 μm), which show a reversal in Sk-d trend (Figure 6c). As an explanation, we suggest that the obvious silicate fracturing including circumchondrule fracturing in Bjurböle (Figure 2g) was caused by a late shock event that resulted in much silicate fracturing. During such fracturing, smaller grains would be created. If fragments broke in such a way as to produce a more heterogeneous distribution of GOS values (some fragments with higher GOS and some with lower GOS), increased GOS skewness would result. Thus, *data for Bjurböle are consistent with a two-stage process: extensive annealing early, probably caused by burial in a warm parent body, and a later shock event that caused fracturing and brought the lithology into a cooler near-surface*

19455100, 0, Downloaded from https://onlinelibrary.wiley.com/doi/10.1111/maps.70246 by ALEX RUZICKA , Wiley Online Library on [09/11/2026]. See the Terms and Conditions (https://onlinelibrary.wiley.com/terms-and-conditions) on Wiley Online Library for rules of use; OA articles are governed by the applicable Creative Commons License

TABLE 4. Deformation style, recovery, recrystallization, and shock-induced melting in lithologies ordered by weighted shock stages (WSS).[a]

	Baszkówka	NWA 7298 Lithology A	Saratov	NWA 7298 Lithology C	Bjurböle	NWA 11351 Lithology A	NWA 11351 Lithology B	NWA 7298 Lithology B	Alfianello	NWA 8709	NWA 4860
WSS	1.07	1.44	1.49	1.72	1.79	3.76	3.87	3.96	4.17	4.62	5.74
Deformation style	Fracturing of sil, tr in matrix	**Sil fracturing; fluidization of bcc**	**Sil fracturing; fluidization of bcc** & tr, bcc twinning	**Sil fracturing;** fluidization of bcc	**Sil fracturing;** fluidization of bcc & tr	**Fluidization of bcc & tr**, 'spotted matrix' vitrification; bcc twinning	**Destruction of chondritic texture;** bcc fluidized & twinned	**Fluidization of bcc & tr**	Fracturing of sil & tr; **plag vitrified**	**Melt matrix formation; fluidization of bcc & tr**; tr & plag veining	**Fluidization of bcc & tr;** melt matrix formation; tr & plag veining
Post-deformation recovery?	Yes ol for $d < 5$; tr, opx	Yes ol locally for $d < 5$	Yes ol, opx, clen for $d < 5$	Yes bcc locally	**Yes ol, opx, tr for $d > 5$**	No	No	No	No	No	No
Recrystallization?	Yes ol, opx	Yes bcc locally, **Yes tr**	No	Yes bcc locally, **Yes tr**	Yes ol locally	Yes tr locally	Yes tr locally	**Yes tr**	**Yes tr, bcc**	**Yes ol**, Yes clen	**Yes ol, opx**
Shock melting?	No	No	No	No	No	Yes meso	Yes meso	Yes melt pockets	Yes melt pockets, veins	**Yes matrix, meso, tr, bcc, plag**	**Yes matrix, meso, tr, plag**

Abbreviations: clen = clinoenstatite; d = equivalent grain diameter in microns; matrix = chondrite matrix; meso = chondrule mesostasis; ol = olivine; bcc = bcc-metal; opx = orthopyroxene; plag = plagioclase; sil = silicates; tr = troilite.

[a]Bolded items are more significant (global in extent) or prominent.

19455100, 0, Downloaded from https://onlinelibrary.wiley.com/doi/10.1111/maps.70246 by ALEX RUZICKA , Wiley Online Library on [09/11/2026]. See the Terms and Conditions (https://onlinelibrary.wiley.com/terms-and-conditions) on Wiley Online Library for rules of use; OA articles are governed by the applicable Creative Commons License

environment. This inference of brittle deformation following annealing in Bjurböle agrees with the conclusions of Soini et al. (2023) based on the study of pores in 3-D with μCT data.

For NWA 7298 Lithology A and C, silicate cataclasis appears to have occurred, and data for larger scale maps show an uptick in GOS Sk values at lower grain sizes (Figure 6). This is inconsistent with post-deformation recovery on the grain size scale of these data (>5 μm). However, smaller scale TM maps obtained at higher spatial resolution show evidence for a decreased Sk value at small (d < 5 μm) grain sizes for olivine in Lithology A of NWA 7298 and for metal in Lithology C of NWA 7298 (Table 4). This suggests that limited annealing after deformation could have occurred for these lithologies analogous to that experienced by Baszkówka and Saratov.

Deformation Effects in Strongly Shocked Chondrites

In strongly shocked chondrites (WSS ~3.8–5.7), there is less of a disparity in GOS values between silicates, metal, and troilite. Elevated GOS values in all minerals are manifested by the presence of numerous low angle grain boundaries. Fluidization textures are still evident for metal and troilite, but shock melting features are also present, ranging from localized melting of chondrule mesostases (NWA 11351 Lithology A and B; NWA 8709, NWA 4860), to localized melting to form melt pockets or veins (NWA 7298 Lithology B, Alfianello), to more extensive melting to create melt matrix (NWA 8709 and NWA 4860). In NWA 8709 and NWA 4860, metal–troilite globules in the matrix of these meteorites are attributed to melting (and therefore fluidization, but in the liquid state) of metal and troilite that is a diagnostic feature of strong impacts in chondritic targets (Hörz et al., 2005; Nakamura et al., 2000). Both meteorites have troilite and plagioclase veins inside chondrule olivine that are attributed to melting and crystallization of these phases after injection or uptake into fractures.

Recrystallization also occurred in the strongly shocked chondrites, with a clear progression that depended on shock stage (Table 4). In the less-shocked (WSS ~ 3.8) NWA 11351 Lithology A and B, troilite and less commonly bcc metal are locally recrystallized, but olivine is not recrystallized. In Alfianello (WSS ~ 4.2), bcc metal and troilite are extensively recrystallized, but again olivine is not recrystallized. In NWA 8709 (WSS ~ 4.6) and NWA 4860 (WSS ~ 5.7), olivine and low-Ca pyroxene in NWA 4860 are now significantly recrystallized, but troilite and metal do not show recrystallization textures. Troilite appears to have been substantially melted to form globules and veins, and bcc metal appears to have been at least partly melted to create globules.

Given that all the strongly shocked chondrites are heavily deformed, recrystallization in them is attributed to strong impact, either dynamic recrystallization occurring during deformation (Lloyd et al., 1997) or static recrystallization caused by elevated heat immediately following impact (Druiventak et al., 2012). However, whether temperatures could stay warm enough for sufficient time to allow static recrystallization to occur while still preserving glass features in the rocks is uncertain. In the most strongly shocked chondrites, melting effects replaced recrystallization as the main process to affect troilite. In these most shocked chondrites, some melting of metal may have occurred, but also martensite was created with deformation character that would have depended on the precise pressure–temperature pathway that was followed (Stöffler et al., 1988). The progressive shock trends observed here generally agree with previous observations (e.g., Bennett & McSween, 1996; Luo et al., 2024; Schmitt, 2000; Stöffler et al., 1988).

None of the strongly shocked chondrites show compelling evidence for post-deformation annealing (Table 4). This suggests *the strongly shocked chondrites experienced relatively fast cooling after shock deformation*. Although evidence in them for subgrain boundaries that might be produced by recovery might be hard to distinguish from numerous subgrain boundaries produced by deformation, recovery is also not evident in GOS skewness data.

Processes Associated with Different Sk-d Patterns

The different lithologies studied here show different olivine Sk-d patterns (Figure 6), and these can be related to recovery, recrystallization, melting, and brecciation effects. The most common pattern observed here and by Ruzicka et al. (2024) is a modest increase in Sk as grain size decreases (Figure 6a). This pattern is shown both by more strongly shocked chondrites (Alfianello, NWA 11351 Lithology A and B, NWA 7298 Lithology B for d > 5 μm) and by weakly shocked chondrites (NWA 7298 Lithology A and C for d > 5 μm). It is attributed to brecciation that creates a more diverse GOS distribution in fragments.

In the more strongly shocked NWA 8709 and NWA 4860 melt breccias, Sk values increase dramatically for smaller grain sizes (d = 5–15 μm and especially d < 5 μm size bins) (Figure 6b). This is certainly attributable to the presence in these meteorites for this size range of both high-GOS grains that record peak deformation as well as low-GOS grains that were recrystallized or formed through melt crystallization. Recrystallized grains in chondrules, clasts, and clumps tend to be small, and grains in the melted matrix are all small. All of these will

19455100, 0, Downloaded from https://onlinelibrary.wiley.com/doi/10.1111/maps.70246 by ALEX RUZICKA , Wiley Online Library on [09/11/2026]. See the Terms and Conditions (https://onlinelibrary.wiley.com/terms-and-conditions) on Wiley Online Library for rules of use; OA articles are governed by the applicable Creative Commons License

have low GOS values. However, unmelted or unrecrystallized deformed grains are still present in this size range, and this will cause a huge dispersion in GOS and therefore a high GOS skewness. Therefore, the large increase in Sk values for small grains ($d < 15$ μm) in NWA 8709 and NWA 4860 is best attributed to partial recrystallization and melting.

The last pattern includes data for the weakly shocked chondrites Baszkówka, Saratov, and Bjurböle (Figure 6c). All three show a decrease in Sk value for decreasing grain size for various grain size ranges, which is attributed to post-deformation recovery operating over different grain size ranges. *Thus, Sk-d data for olivine can be used to identify the relative importance of different processes and the scales over which they occur*.

Thermomechanical Histories for Different Lithologies

Baszkówka

We attribute both localized recrystallization and recovery in Baszkówka to a static annealing process that accompanied the burial of warm materials. A similar interpretation was suggested by Krzesińska and Almeida (2019). The large voids in Baszkówka could have been gas-filled voids, explaining circular pores in matrix as vesicles. Vapor could transport species to result in condensation, producing well-formed crystal faces adjacent to pores (Krzesińska & Almeida, 2019) and allowing bridging crystals to form. To explain fragments in matrix and some bcc metal grains that are martensitic in texture, earlier brecciation and relatively rapid cooling of metal from a higher temperature could have occurred prior to agglomeration.

Although Krzesińska and Almeida (2019) suggested that a strong impact on an asteroidal body could have produced an impact plume followed by re-agglomeration of warm materials, *we favor the formation of Baszkówka by a weak impact on an already warm parent body leading to a warm ejecta deposit*. Although there is good evidence for materials being warm after agglomeration leading to minor recovery and recrystallization, most crystals are undeformed, making a strong impact unlikely. Moreover, the recovery scale implied by Sk-d data for olivine is <5 μm, too small to remove all deformation from coarser olivine, and evidence for recrystallization in coarser grains is lacking. If re-agglomeration occurred in the presence of gas (possibly degassed from the parent body), fine and coarse particles would settle at different rates and could become separated, possibly explaining why so little matrix occurs in Baszkówka. Gas could become trapped during agglomeration to form vugs. Elevated $R_{2\text{-}10}$ and T_{deform} values for Baszkówka (Table 3) resemble those of other weakly shocked chondrites (Figure 7; Ruzicka et al., 2024) and are plausibly attributed to accretionary processes as T_{deform} values (~910 °C) (Table 3) are too high to be consistent with the type 5 metamorphic grade (e.g., ~700–750 °C as estimated by Hutchison, 2004; ~675–865 °C for type 4 or 5 as reviewed by Harrison & Grimm, 2010). However, temperatures could still have been elevated in the parent body and consistent with type 5 grade at the time of a weak impact event, as weak shocks leave $R_{2\text{-}10}$ values nearly unchanged (Ruzicka et al., 2024). An old $^{40}Ar/^{39}Ar$ plateau age of 4505 ± 21 Ma for Baszkówka (Friedrich, Rubin, et al., 2014) is consistent with a parent body that experienced early heating and degassing.

Saratov and Bjurböle

Both Saratov and Bjurböle show good evidence for dominantly brittle deformation in silicates to produce fractures across and around chondrules and small matrix fragments, and a more ductile deformation in metal and troilite, although troilite experienced some fracturing (Table 4). Both meteorites show evidence for recovery but in different ways; Saratov experienced minor annealing following silicate fracturing, whereas Bjurböle was significantly annealed and then experienced fracturing. Both meteorites have elevated $R_{2\text{-}10}$ implying elevated deformation temperatures for olivine ($T_{deform} \sim 920$–960 °C, Table 3), which are probably too high to be consistent with the type 4 metamorphic grade of the meteorites (~600–700 °C as estimated for type 4 by Hutchison, 2004; ~675–865 °C for type 4 or 5 as reviewed by Harrison & Grimm, 2010). Note that this differs from the interpretation for some weakly shocked H4 chondrites made by Goudy et al. (2023), who attributed elevated $R_{2\text{-}10}$ values to high metamorphic temperatures at the time of shock. Instead, high $R_{2\text{-}10}$ values for the various weakly shocked type 4 lithologies are probably a signature of accretion under warm conditions, as seen for other weakly shocked type 3 chondrites (Ruzicka et al., 2024). Thus, *Saratov and Bjurböle were affected by weak impacts occurring on warm parent bodies that were being annealed before (Bjurböle) and after (Saratov) deformation*. This idea of annealing occurring both after and before shock deformation in different ordinary chondrites was suggested by Rubin (2004) and by Goudy et al. (2023). However, both Saratov and Bjurböle were considered to have been annealed after shock (Rubin, 2004). In any case, old $^{40}Ar/^{39}Ar$ ages for Saratov (4400 ± 30 Ma; Turner et al., 1978; Swindle et al., 2014) and Bjurböle (4588 ± 23 Ma based on 580–1000 °C heating steps; Turner, 1969) are consistent with early heating and deformation events.

Northwest Africa 7298

Lithology B of NWA 7298 was strongly shocked with much plastic deformation of silicates (CSS = S4) (Table 3).

19455100, 0, Downloaded from https://onlinelibrary.wiley.com/doi/10.1111/maps.70246 by ALEX RUZICKA , Wiley Online Library on [09/11/2026]. See the Terms and Conditions (https://onlinelibrary.wiley.com/terms-and-conditions) on Wiley Online Library for rules of use; OA articles are governed by the applicable Creative Commons License

The stronger deformation of Lithology B compared to Lithology A within which it is enclosed can be explained if Lithology B was shocked in an earlier impact.

Although the three lithologies in NWA 7298 were shocked to different intensities (more in Lithology B than in Lithologies A and C), all were probably shocked when their protoliths were warm. For Lithologies A and C, the best evidence for this is the presence of recrystallized troilite which can be explained by dynamic recrystallization in a weak shock event that affected warm materials. Similarly, we speculate that two distinctive features of metal in NWA 7298 Lithology A and C—the highest GOS values and a low <111> twinning proportion—could be because of high ambient temperature during impact processing. The best evidence for a warm protolith for Lithology B is the combination of high $R_{2\text{-}10}$ (or high T_{deform}) values as well as high olivine GOS (Figure 7), attributed to a strong shock occurring on a warm body. Olivine T_{deform} values (~960–990 °C) for NWA 7298 Lithology A and C are high (Table 3) and probably were largely inherited from an earlier warm accretion epoch, because such high temperatures seem incompatible with the relatively low metamorphic grades of these lithologies (type 3–4 for Lithology A, with metamorphic temperatures for type 3 of ~260–600 °C according to Huss et al., 2006; and type 5 for Lithology C). Thus, the data for NWA 7298 Lithology A and C are best accommodated by early warm accretion and impact processing while the parent body was warm but not as hot as implied by T_{deform}.

Therefore, *NWA 7298 was formed by at least two and maybe more impact events on a warm parent body: an early strong shock to create Lithology B, and one or more weaker shocks to create Lithology C and A and assemble the breccia*. Except for having a warm parent body, this conforms to the model for NWA 7298 suggested by Friedrich, Weisberg, et al. (2014). As Lithology C is type 5 metamorphic grade and present as a clast within lower type Lithology A, the assembly of the breccia must have occurred during or after the thermal metamorphism experienced by Lithology C.

Northwest Africa 11351

In contrast to NWA 7298, the genomict breccia that is *NWA 11351 was assembled by a strong impact event that probably occurred under cool ambient conditions*. μCT data for metal grains in all three lithologies (A, B, C) of NWA 11351 imply that they were foliated in one shock event (Ruzicka et al., 2024). Similarly, average $GOS_{d>50}$, $R_{2\text{-}10}$ and Sk values for olivine in Lithology A and B are notably similar (Figures 6 and 7), consistent with one shock event. As Lithology C is itself a genomict breccia that contains type 5 grade clasts (Ruzicka et al., 2024), the strong impact event that assembled the NWA 11351 breccia must have occurred after type 5 thermal metamorphism. T_{deform} values (~730–750 °C) for Lithologies A and B in NWA 11351 resemble other strongly shocked meteorites and are interpreted as shock-reheating temperatures from an ambient cool pre-shock state. Partial recrystallization of troilite and metal and melting effects are attributed to the strong shock. We speculate that shearing may have been responsible for the almost complete destruction of chondritic texture in Lithology B, and that well-developed <111> twins in bcc metal of both Lithologies A and B were produced by relatively high shear stress, high strain rate, and low temperatures during deformation.

Alfianello

Among other strongly shocked chondrites in this study, Alfianello has the highest μCT fabric strength parameter (C) for metal, the highest porosity, slightly low average $R_{2\text{-}10}$ for olivine, and unusually low $GOS_{d15\text{-}50}$ values for bcc metal and troilite (Figure 1). The first two features seem incompatible with one another, and the slightly high porosity value might indicate a difference in the way this sample was compacted compared to other strongly shocked chondrites. The low $R_{2\text{-}10}$ implies a low deformation temperature, and the low GOS values for metal and troilite can be readily explained by pervasive recrystallization during intense shock, which also produced localized melting (Table 4). *Alfianello was thus strongly shocked on a cool parent body*, in a relatively late impact suggested by a young $^{40}Ar/^{39}Ar$ plateau age (1050 ± 50 Ma) (Kunz et al., 1997).

NWA 8709

This type 3 melt breccia records a strong impact that melted interstitial regions between chondrules. It shows how chondrites can be transformed into impact melt rocks through a combination of deformation, recrystallization, and melting.

Matrix formed by crystallization from the interstitial melt and is dominated by pigeonite, suggesting a pyroxene-rich composition for the melt. The common association of bcc metal and troilite in matrix globules suggest these were partly formed by immiscible separation of a metallic melt from a silicate melt. Significant impact-induced (dynamic?) recrystallization was responsible for creating the low-GOS olivine domains amidst deformed olivine grains in small chondrules and clasts (Figure 3f) but was also important for fine-grained olivine-rich clumps (Figure 3g). The clumps are dominated by olivine that could have largely recrystallized but also contain glass and minerals that could have formed by secondary solidification of a melt interstitial to olivine. The fine-grained olivine borders that surround some chondrule clasts (Figure 3f) are

19455100, 0, Downloaded from https://onlinelibrary.wiley.com/doi/10.1111/maps.70246 by ALEX RUZICKA , Wiley Online Library on [09/11/2026]. See the Terms and Conditions (https://onlinelibrary.wiley.com/terms-and-conditions) on Wiley Online Library for rules of use; OA articles are governed by the applicable Creative Commons License

interpreted as partially recrystallized, peripherally melted chondrules. The moderately low $R_{2\text{-}10}$ value for NWA 8709 despite strong shock (Figure 7) implies shock reheating from a low ambient temperature. Thus, *NWA 8709 was strongly shocked on a cool parent body probably close to the zone of maximum deformation and heating* (e.g., Stöffler et al., 2018) *within an impact crater*.

NWA 4860

This meteorite experienced an intense shock to result in significant impact-induced (dynamic?) recrystallization of olivine. Bcc-metal in this meteorite is composed of chemically uniform martensite that was probably homogenized at high temperature and then cooled in disequilibrium below the martensite start temperature (Schepker, 2014). This disequilibrium could have occurred due to rapid cooling (Mao et al., 2018; Mushnikov et al., 2022) or a nucleation difficulty (Reisener & Goldstein, 2003a, 2003b). Some metal could have melted to explain metal–troilite globules in the melt matrix, but larger grains show evidence only for fluidization, not necessarily melting. The large number of vugs was probably generated by impact vaporization that filled cavities with gas, and vug crystals could have formed by condensation possibly in the presence of some melt, as has been proposed for other strongly shocked, vuggy chondrites (Fruland, 1975; Olsen, 1981; Xie & Chen, 1997).

A striking feature of NWA 4860 is the relative uniformity in crystal orientation of troilite (Figure 3k). This can be explained in different ways.

1. Troilite may have crystallized from an interstitial melt. This process was suggested to account for mm-sized oikocrysts in Portales Valley (Ruzicka & Hugo, 2018). In NWA 4860, orientation domains are ~2–4 mm across, suggesting oikocrysts this large. Melting and crystallization would explain the weak deformation of troilite, as it would have crystallized following peak shock pressure and deformation. Presumably, grains crystallizing from liquid would grow epitaxially on one another to obtain similar orientations. However, one problem is that the subhedral troilite that overgrew metal in a vug (Figure 3i) has the same orientation as in the adjacent host rock and more likely condensed from a gas.
2. Troilite may have been reoriented by crystal plastic deformation. Although beyond the scope of this study, the dominant slip system for troilite in NWA 4860 that can be inferred from EBSD data would be consistent with the preferred orientation of troilite if compression were almost in the (observed) X-Y plane. One significant problem with this idea is that troilite is weakly deformed and not recrystallized, but it should be strongly deformed or recrystallized if crystal plasticity controlled the orientation of grains.
3. The troilite may have condensed from gas. This can better explain the presence of vug troilite. However, in most areas, troilite is not associated with voids in the plane of the section. At least one other prominent troilite grain occurs adjacent to a void, but most grains are not associated with obvious vugs. Of course, vugs would not be visible if they occur outside the X–Y plane, but a large fraction should appear to be associated with vugs if condensation was dominant. Furthermore, condensation alone would not explain the preferred orientation. One would still need to appeal to epitaxial growth.

On balance, we favor the first idea that most troilite crystallized from a melt. Gas likely coexisted with melt and could have condensed inside vugs. It is possible that, prior to melting, plastic deformation aligned the troilite, and that afterward, troilite crystallized epitaxially on unmelted remnants thereby explaining the specific preferred orientation. To explain how the vug troilite can have the same crystal orientation despite having grown from vapor, we suggest that it epitaxially nucleated on troilite in the adjacent host in an area outside the X–Y plane of the section.

As was the case for NWA 8709, the moderately low $R_{2\text{-}10}$ value for NWA 4860 despite strong shock (Figure 7) implies shock reheating from a low ambient temperature. Thus, the preferred interpretation is that *NWA 4860 was affected by an intense shock on a cool parent body close to the maximally heated and deformed area in an impact crater, resulting in widespread melting of the troilite followed by epitaxial growth to create mm-sized grains and producing gas-filled vugs that condensed minerals*.

Warm Chondrule Accretion or Impacts on Warm Bodies?

All weakly shocked chondrites (Baszkówka, Saratov, Bjurböle, NWA 7298 Lithology A, NWA 7298 Lithology C) as well as the strongly shocked Lithology B of NWA 7298 have evidence for deformation occurring at elevated temperatures (T_{deform} values of ~910–997 °C, with estimated accuracies of ~86–99 °C; Table 3). For none of these weakly shocked lithologies are the elevated temperatures the result of shock heating per se, as they are all far too weakly deformed to experience appreciable shock heating (Ruzicka et al., 2024; Schmitt, 2000; Stöffler et al., 1988, 2018). Instead, high temperatures can be explained by one of two processes: (1) impacts on warm parent bodies, in which the high temperature signature reflects elevated pre-shock temperature, or (2)

19455100, 0, Downloaded from https://onlinelibrary.wiley.com/doi/10.1111/maps.70246 by ALEX RUZICKA , Wiley Online Library on [09/11/2026]. See the Terms and Conditions (https://onlinelibrary.wiley.com/terms-and-conditions) on Wiley Online Library for rules of use; OA articles are governed by the applicable Creative Commons License

high temperatures of material (chondrules) accreting in planetesimals. Ruzicka et al. (2024) studied type 3 ordinary chondrites and concluded that chondrules preserve a nebular signature of cooling from melt temperatures and accreting in planetesimals while still warm (final accretion temperature ~ 900–950 °C). They inferred that this warm accretion signature would persist for all weakly shocked (S3 or less) chondrites.

For the weakly shocked (S1 or in one case S2) chondrites studied here, there are three main arguments to consider: (1) whether T_{deform} values can be explained solely or in part by metamorphic heating, (2) whether there is evidence that ambient temperatures on a parent body were high at the time of a later impact, and (3) whether there is any evidence for post-deformation annealing such as might occur in a warm parent body.

We found evidence for *both* warm parent body deformation as well as accretion of warm chondrules for all the weakly shocked chondrites, as detailed earlier in this discussion and summarized here. (A) Elevated T_{deform} values all point to the importance of at least some inheritance from accretion, as metamorphic temperatures in type 3–5 lithologies were probably too low to be consistent with T_{deform} values. This is more true for type 4 Bjurböle and Saratov and type 3 Lithology A in NWA 7290, but probably also true for type 5 Baszkówka and Lithology C in NWA 7290. (B) On the other hand, there is good evidence that the parent body for NWA 7290 was warm at the time of impacts, based on the prevalence of recrystallized troilite despite weak deformation in olivine for NWA 7290 Lithology A and C, a mismatch that is best explained by elevated ambient temperatures at the time of shock (Schmitt, 2000). (C) Finally, all the weakly shocked lithologies show evidence for recovery and/or recrystallization features (Table 4), consistent with post-deformation annealing that can be explained by burial in warm materials (warm parent body). Thus, for the weakly shocked chondrites, impacts occurred on parent bodies that were undergoing metamorphic heating, but all also preserved a signature for nebular processes involving hot and cooling chondrules.

Grouping of Chondrite Lithologies According to Key Parameters

Figure 8 shows olivine $R_{2\text{-}10}$ versus GOS skewness ratio $Sk_{d>50}/Skd_{5\text{-}15}$ for different lithologies and serves as a useful guide to key aspects of the deformation-thermal histories of the lithologies. As will become apparent, these parameters are largely independent of petrographic type and metamorphic grade. $R_{2\text{-}10}$ is related to deformation temperature and $Sk_{d>50}/Skd_{5\text{-}15}$

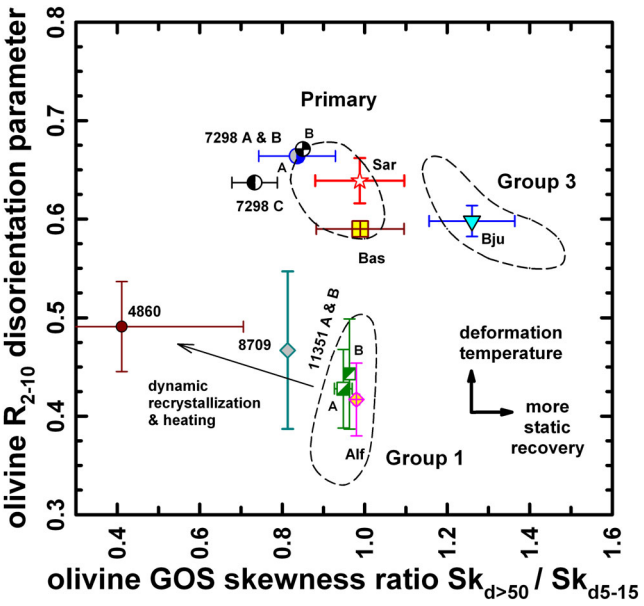


FIGURE 8. Olivine $R_{2\text{-}10}$ versus GOS skewness ratio for different grain sizes ($Sk_{d>50}/Sk_{d5\text{-}15}$). Fields for Group 1, Group 3, and Primary Group are from Ruzicka et al. (2024). A large error bar for Sk ratio for NWA 8709 (Table 3) is omitted for clarity. Meteorite labels as in Figure 4.

can distinguish between annealed (>1) and non-annealed (≤1) cases (Ruzicka et al., 2024). Because GOS skew data in Figure 8 include only d > 5 μm grains, Figure 8 is not sensitive to effects seen only in small grains, and thus, the data in Figure 8 pertain to larger scale features in the meteorites.

Bjurböle fits within the "Group 3" field (Figure 8). Meteorites in this field, such as Portales Valley, Kernouvé, and Miller Range 99301, show good evidence of having been shocked at elevated temperature and then significantly annealed, probably by deep burial after impacts on warm parent bodies (Ruzicka et al., 2005, 2015, 2024; Ruzicka & Hugo, 2018). Aside from Bjurböle, the known examples of Group 3 are type 6 chondrites, and this high metamorphic grade fits with the idea that they could have been significantly annealed, but Bjurböle is classified as a lower grade type 4 chondrite. A type 4 designation for Bjurböle is consistent with Huss et al. (2006) based on the mineralogy of d ≥ 2–10 μm grains as determined with EBSD in larger maps (LAM, DM1, DM2): <1 area% plagioclase, and appreciable amounts of clinoenstatite (clen) compared to orthopyroxene (opx), with clen/[clen+opx] ~0.2–0.3 by area. Thus, it appears that significant olivine annealing can occur even for type 4 grade.

NWA 7298 Lithology A, Saratov, and Baszkówka are type 3/4, type 4, or type 5 chondrites (respectively) that fit within the "Primary Group" (Figure 8). This

19455100, 0, Downloaded from https://onlinelibrary.wiley.com/doi/10.1111/maps.70246 by ALEX RUZICKA , Wiley Online Library on [09/11/2026]. See the Terms and Conditions (https://onlinelibrary.wiley.com/terms-and-conditions) on Wiley Online Library for rules of use; OA articles are governed by the applicable Creative Commons License

group includes weakly shocked type 3 chondrites that appear to record an early thermal signature, interpreted to reflect the accretion of warm chondrules (Ruzicka et al., 2024). NWA 7298 Lithology C probably also belongs to this group, although it has an unusually low value for $Sk_{d>50}/Skd_{5\text{-}15}$ (Figure 8). This low ratio indicates less GOS dispersion for coarser (d > 50 μm) than finer (d = 5–15 μm) grains (as indicated also in Figure 2a), which could be caused by shattering of grains during impact into smaller fragments that have varied GOS values.

Although NWA 7298 Lithology B appears in Figure 8 to also fit with the primary group, it is different in that it was strongly deformed, which would have overprinted an earlier deformation signature (Ruzicka et al., 2024), and instead appears to have been shocked at an elevated ambient temperature. As the lithology was not significantly annealed following deformation, GOS skewness ratio did not increase. Thus, the proximity of Lithology B to the Primary Group in Figure 8 belies the significant shock processing it experienced.

Alfianello (type 6) and Lithologies A and B from NWA 11351 (type 3/4) fall within the "Group 1" field (Figure 8). Other meteorites in this group include strongly shocked L6 and LL6 chondrites (Leedey, Bruderheim, Morrow County, Elbert) (Hugo et al., 2020; Ruzicka et al., 2024). These meteorites show good evidence of having been shocked from low ambient temperature with no appreciable annealing after deformation (Hugo et al., 2020; Ruzicka et al., 2015; Ruzicka & Hugo, 2018), and the same is likely true for Alfianello and NWA 11351.

The strongly shocked melt breccias NWA 4860 (type 4) and NWA 8709 (type 3) lie significantly outside the established fields (Figure 8). They appear to be on a trajectory from Group 1 meteorites involving a large decrease in GOS skewness ratios and a small increase in $R_{2\text{-}10}$ values (Figure 8). This trajectory can be explained by more recrystallization and shock heating compared to Group 1. Recrystallization during intense shock creates low-GOS grains in addition to heavily deformed high-GOS grains but only affected the smaller (d = 5–15 μm) grain population and not the larger grain population (d > 50 μm), as recrystallization makes smaller grains from larger precursors. This leads to high $Sk_{d5\text{-}15}$ values and low $Sk_{d>50}/Sk_{5\text{-}15}$ ratios. Stronger shocks lead to higher shock and post-shock temperatures (e.g., Melosh, 1989; Schmitt, 2000; Sharp & DeCarli, 2006; Stöffler et al., 1988) and should lead to higher $R_{2\text{-}10}$ values recorded by the deformed olivine grains. NWA 4860 lies farther from the Group 1 field than NWA 8709 because it was more intensely shocked. The average $R_{2\text{-}10}$ values for NWA 8709 and NWA 4860 correspond to model deformation temperatures (T_{deform}) of ~775 and ~800 °C, respectively (Table 3). *This suggests that for cool protoliths ~ 775–800 °C is close to the maximum shock reheating temperature for olivine grains, although this does not preclude locally higher temperatures elsewhere or for more intensely shocked (*e.g., *melt) rocks.*

Varied Deformation Response of Olivine, FeNi-Metal, and Troilite

The data presented here indicate a large difference in the shock response of olivine, bcc metal, and troilite. Specifically, three observations require explanation. Observation 1 is that, in weakly shocked chondrites, there is a dominance of brittle deformation in olivine and other silicates as evidenced by dominant fracturing and cataclasis, but in metal and troilite, there is less fracturing and more evidence for plasticity, including textures that indicate fluidization of metal and troilite (Table 4). Observation 2 is that, in weakly shocked chondrites, average $GOS_{d15\text{-}50}$ values increase in the sequence of olivine < troilite < metal, entailing GOS ratios of metal/olivine ~2.7–7.6 and troilite/olivine ~1.3–4.8 (Figure 4a). Observation 3 is that, for the entire sample suite, average $GOS_{d15\text{-}50}$ ratios for metal/olivine and troilite/olivine generally decrease with increasing shock intensity (olivine $GOS_{d>50}$ or $GOS_{d15\text{-}50}$) (Figure 4b).

To interpret these data, it is helpful to first recognize that average GOS in deformed materials is a metric related to overall strain (Ayad et al., 2012; Bouquerel et al., 2021; Brewer et al., 2009; Fujiyama et al., 2011; Kang et al., 2007; Wright et al., 2011). In steel, for instance, the tangent of average GOS (in radians) resembles the value of strain measured for the steel (Bouquerel et al., 2021; Kang et al., 2007). This expression for GOS likewise resembles the expression for engineering shear strain or true simple shear strain (e.g., Lubliner, 2006; Pardis et al., 2017). The rough equality implies that GOS relates mainly to *shear strain*. Indeed, solids are susceptible to deformation by shear stresses during shock (Melosh, 1989), and shear stress will cause distortions in crystal lattices that can be recorded as intragranular misorientation. Thus, *shear stress during impact is likely to have been important in affecting GOS*. This shear stress will be generated even with uniaxial shock waves because of the longitudinal and perpendicular stresses that are part of a shock wave (Melosh, 1989).

To explain Observation 1, we suggest that *the weakly shocked chondrites experienced shear stresses determined by the Hugoniot Elastic Limit (HEL) of the minerals*. HEL is the point on the Hugoniot at which plastic yielding occurs and the point where material failure is determined by plastic distortion rather than by microcracking (Melosh, 1989; Thomas et al., 2018). HEL therefore reflects a brittle–ductile transition. It equates to

19455100, 0, Downloaded from https://onlinelibrary.wiley.com/doi/10.1111/maps.70246 by ALEX RUZICKA , Wiley Online Library on [09/11/2026]. See the Terms and Conditions (https://onlinelibrary.wiley.com/terms-and-conditions) on Wiley Online Library for rules of use; OA articles are governed by the applicable Creative Commons License

a longitudinal stress that is related to the yield stress Y, which marks the shear stress where plastic flow begins for a total shock pressure P (Melosh, 1989). Experimental data indicate that, for α iron (low pressure) bcc metal, the HEL is ~0.9 GPa (Thomas et al., 2018), and that, for olivine (forsterite), the HEL is ~7–11 GPa depending on crystal orientation (Syono et al., 1981) with a precise 7.44 GPa HEL measured for forsterite in the <001> direction (Obata et al., 2023). The HEL estimated for troilite is ~3.5 GPa, based on data for yield stress and Poisson's ratio for the related mineral pyrrhotite given by Moreau et al. (2018). This means that, during shock, bcc metal achieves plasticity at lower shear stress and shock pressure than troilite, which in turn achieves plasticity at lower stress and shock pressure than olivine. Thus, if stress was mostly above the HEL values for bcc metal and troilite grains and mostly below the HEL values for olivine grains, metal and troilite would be dominantly plastic while olivine would be dominantly brittle, consistent with Observation 1. Thus, assuming that the experimental data can be applied directly to natural shocks (see Sharp and DeCarli (2006), Smith et al. (2016), Cheng et al. (2021), and Singla and Ray (2022) for potential complications), *the weakly shocked chondrites could have experienced stresses of ~4–7 GPa. A corollary is that the strongly shocked chondrites experienced stresses > 7 GPa*. Furthermore, it appears that GOS values for the three minerals are related to their Hugoniot Elastic Limit. The ratios of HEL values for the minerals are inversely related to $GOS_{d15\text{-}50}$ values for the weakly shocked meteorites: $olivine_{HEL}/metal_{HEL} \sim 8.2$ and $olivine_{HEL}/troilite_{HEL} \sim 2.1$ (assuming for olivine a 7.44 GPa HEL), compared to $metal_{GOS}/olivine_{GOS} \sim 2.7–7.6$ and $troilite_{GOS}/olivine_{GOS} \sim 1.3–4.8$. This quantitative semi-agreement implies that GOS is recording differences in strain that are related to the yield stresses of the minerals, with the lower yield stress for bcc metal allowing more strain to accumulate in metal, the higher yield stress for olivine allowing less strain to accumulate in olivine, and troilite intermediate. Thus, *it appears that GOS values for minerals in the weakly shocked chondrites also can be explained by differences in yield stress*, explaining Observation 2.

The systematic decrease in the GOS ratios bcc/olivine and troilite/olivine with increasing olivine GOS (Figure 4b, Observation 3) is caused both by an increase in GOS for olivine and by steady or decreasing GOS values for metal and troilite (Figure 4a). For instance, in the sequence of increasing olivine GOS going from Bjurböle to NWA 11315 Lithology A and B, NWA 7298 Lithology B, NWA 4860, and finally to NWA 8709 (a factor of >2 increase in olivine GOS), bcc metal has quasi-constant or slightly decreasing $GOS_{d15\text{-}50}$ values (Figure 4a). In the strongest shocks, melting processes are responsible for low GOS values in troilite, and recrystallization was responsible for the low GOS values in metal and troilite in Alfianello, but an additional process must be invoked to explain the overall GOS trend for bcc/olivine and troilite/olivine.

The GOS data are interpreted to reflect a strain "softening" process (strain decreasing with increasing shear stress) for bcc metal and troilite. The traditional explanation for such softening in minerals is recrystallization or recovery (Lubliner, 2006; Van der Pluijm & Marshak, 2004; Vernon, 2018), but except for Alfianello, recrystallization of bcc metal and troilite is not very evident in the strongly shocked chondrites. This leaves recovery as the better explanation. Unlike static recovery that occurred after deformation, we suggest that *a "dynamic recovery" process* (Zeuch & Green II, 1984) *occurred for bcc metal and troilite, in which dislocations are annihilated by dislocation climb during deformation*, and that this can explain Observation 3. Such climb is promoted at higher temperatures that would accompany stronger shocks, so more recovery would occur in stronger shocks, and this could partly explain the trend for decreasing bcc/olivine and troilite/olivine GOS with increasing shock intensity shown in Figure 4b. For dynamic recovery, some dislocations would be removed by recovery, but some would be added by ongoing deformation. This might make it difficult or impossible to easily identify recovery in these deformed grains from EBSD map images alone. Dynamic recovery can be inferred for metal and troilite because of the comparison with olivine where the process was less active.

However, there is evidence for dynamic recovery in olivine as well, at least for the most strongly shocked chondrite (NWA 4860), as can be seen by comparison to the next most strongly shocked chondrite (NWA 8709). Comparing data only for *non-recrystallized grains* with GOS > 1° in the LAM maps for the two chondrites, average $GOS_{d>50} = 5.9° \pm 2.1°$ (Ng = number of grains = 321) in NWA 4860, and average $GOS_{d>50} = 6.6° \pm 2.7°$ (Ng = 712) in NWA 8709. The lower value of the former can be attributed to dynamic recovery that lowered strain. This recovery accompanied olivine recrystallization, which owing to stronger shock was more advanced in NWA 4860 (based on LAM data, the recrystallized fraction with GOS < 1° is ~47% —Figure 3h) than in NWA 8709 (recrystallized fraction ~13%).

To summarize the inferences above, differences in brittle-ductile deformation behavior for olivine, bcc metal, and troilite during weak shock were caused by differences in the yield strengths of the minerals. This allowed different amounts of strain to accumulate in them (most for metal, intermediate for troilite, least for olivine), with

19455100, 0, Downloaded from https://onlinelibrary.wiley.com/doi/10.1111/maps.70246 by ALEX RUZICKA , Wiley Online Library on [09/11/2026]. See the Terms and Conditions (https://onlinelibrary.wiley.com/terms-and-conditions) on Wiley Online Library for rules of use; OA articles are governed by the applicable Creative Commons License

these different amounts of strain manifested by GOS values. As shock intensity increased, metal and troilite experienced dynamic recovery even as plastic deformation in olivine became more important. This caused trends in GOS to diverge (increasing GOS for olivine, quasi-steady or declining GOS for metal and troilite) until recrystallization and melting occurred in troilite and metal; ultimately, olivine itself underwent (dynamic?) recrystallization and dynamic recovery.

Finally, shock pressures can be estimated for the weakly shocked and strongly shocked chondrites based on the stresses estimated for olivine, bcc metal, and troilite. Mean shock pressure P at plastic yielding can be calculated from the expression:

$$P = \mathrm{HEL}/2 \times [1 + 2 \times (\gamma/(1-\gamma))] \quad (1)$$

found by combining (1) the expression for longitudinal stress ($\sigma_L = \mathrm{HEL}$ at yielding) and the perpendicular stress (σ_P) that are related by Poisson's ratio (γ), given by $\sigma_P = (\gamma/(1-\gamma)) \times \sigma_L$, and (2) the expression for mean pressure $P = (\sigma_L + 2\ \sigma_P)/2$ (Melosh, 1989). With values for Poisson's ratio of 0.292 for bcc metal (Thomas et al., 2018), 0.25 for troilite (Moreau et al., 2018), and 0.24 for olivine (Christensen, 1996), and the HEL values given above, mean pressures at plastic yielding for bcc metal, troilite, and olivine are ~0.8, ~2.9, and ~6.1 GPa, respectively. This implies that the weakly shocked chondrites (which have CSS = S1-S2) were shocked to mean pressures of ~2.9–6.1 GPa and the strongly shocked chondrites (CSS = S4-S6) were shocked to mean pressures of >6.1 GPa. These pressure ranges overlap with those estimated by Stöffler et al. (2018) for the weakly shocked S1 (<4–5 GPa) and S2 chondrites (<5–10 GPa) and are not inconsistent with the more strongly shocked S4 (>10–20 GPa) and S5 and S6 chondrites.

Implications for Lithification

A significant difference occurs between weakly shocked and strongly shocked lithologies regarding the style of deformation, and this has implications for how lithification occurred.

In the weakly shocked lithologies, features that inhibited lithification (silicate cataclasis, minimal shock compression and shock heating) were counteracted by features that promoted lithification, such as fluidization of metal and troilite during impact (Table 4) and deformation on already warm parent bodies. For fluidized metal and troilite and their surroundings, fractures are absent in metal, few in troilite, and largely absent in surrounding silicates, although silicates are heavily fractured elsewhere. This suggests that fluidized materials filled voids and acted as binding agents that helped attach silicates to them. Binding was also promoted by metamorphic annealing and grain growth on warm parent bodies (Guignard & Toplis, 2015).

In the strongly shocked lithologies, different features promoted lithification, including more shock-induced compression and heating, and even melting, along with continued fluidization of metal and troilite (Table 4). The only feature working against lithification in the strongly shocked lithologies was low ambient temperature before and after shock, restricting the amount of possible sintering.

The existence of both types of shocked chondrites implies formation under conditions that did not result in the pulverization of parent asteroids and their complete dispersal into space, which requires low impact velocities (Hartmann, 1979; Stöffler et al., 1988). This leads us to suppose that some lithification occurred by cratering episodes on largely intact parent bodies. However, lithification might still be possible if the parent bodies were disrupted and reassembled under warm conditions, such as might occur if the parent bodies were already warm at the time of impact. In contrast, extensive disruption of a cool parent body and re-accretion of gravitationally bound rocks would probably not lead to lithification, but rather to a loose rubble pile.

For the chondrites in this study, we suggest three types of chondrite lithification settings at different times, two of which involve cratering on low-gravity asteroidal bodies. We consider cratering mechanics and observations (e.g., Melosh, 1989; also Stöffler et al., 2018 and Tomkins, 2009) that indicate two broad types of impact products: "intracrater" materials that include floors, subfloors, and walls where material has been displaced and pressed into the target body, and "fallback" materials that will be lofted as ejecta and re-accreted as fallback around the crater or within it. We expect intracrater materials to mostly have been more compressed than fallback materials, especially if fallback involved re-accretion after collisional disruption, although collapse of crater walls could result in lower porosity crater materials, and ejecta could include blocks of more compacted materials. For parent body sizes of the ordinary chondrites, we envision diameters of order ≥200 km (e.g., Blackburn et al., 2017; Harrison & Grimm, 2010; Noonan et al., 2019; Rubin, 2026).

Figure 9 shows lithification settings for ordinary chondrites and their chondrules. In **Setting A**, initial lithification of chondritic aggregates for ordinary chondrites is inferred to have occurred under warm accretion conditions resulting in chondrule clumps that produced cluster chondrite textures, assemblages of tightly-fitting chondrules (Metzler, 2012; Ruzicka et al., 2024) and well shown by Lithology A in NWA

19455100, 0, Downloaded from https://onlinelibrary.wiley.com/doi/10.1111/maps.70246 by ALEX RUZICKA , Wiley Online Library on [09/11/2026]. See the Terms and Conditions (https://onlinelibrary.wiley.com/terms-and-conditions) on Wiley Online Library for rules of use; OA articles are governed by the applicable Creative Commons License

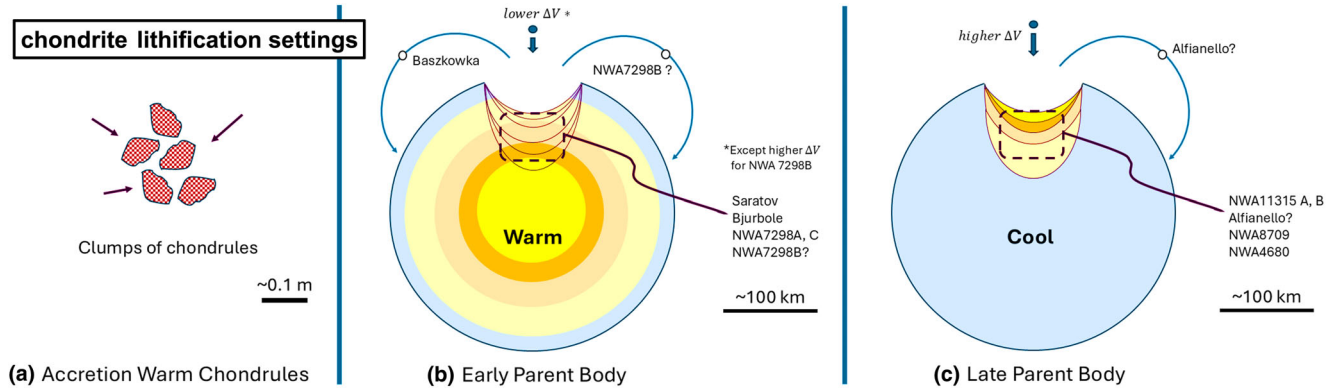


FIGURE 9. Schematic showing proposed chondrite lithification settings. **Setting A**: Accretion of warm chondrules forms aggregates with cluster chondrite texture, which are best preserved texturally in some type 3 ordinary chondrites but which is also preserved in the $R_{2\text{-}10}$ signature of olivine in weakly shocked chondrites. **Setting B**: Mostly low-velocity (lower ΔV) impacts produce craters on H, L, and L/LL parent bodies undergoing metamorphism, which compress materials beneath the impact craters to form the weakly shocked chondrites Saratov (H4), Bjurböle (L/LL4), and NWA 7298 Lithology A and C (H3-5). Baszkówka (L5) and Lithology B of NWA 7298 (H4) may have formed in a similar setting or as ejecta that was redeposited on the surface. Warmer colors toward the center of the parent body represent increasing metamorphic temperatures. **Setting C**: Higher velocity (higher ΔV) impacts produce craters on cool L and LL parent bodies, which compress and heat materials beneath the impact craters to form the strongly shocked chondrites NWA 11351 Lithology A and B (LL3-4), and the melt breccias NWA 8709 (L3) and NWA 4860 (L4). Alfianello (L5) may have formed in a similar setting or as ejecta that was redeposited on the surface. Warmer colors towards the top of crater floor represent increasing shock-reheating temperatures. Note that sketches here for impact craters (Settings B and C) exclude intracrater fallback and slump materials (see Tomkins, 2009).

11351. Surviving clasts of these aggregates are up to a decimeter across (Metzler, 2012; Ruzicka et al., 2024) and may have been larger initially. Warm chondrules accreted at an estimated final temperature of ~900–950 °C (Ruzicka et al., 2024), which compares favorably to the weakly shocked lithologies with T_{deform} values of ~909–989 °C (Table 3), supporting the idea that olivine in weakly shocked chondrites record the original accretion conditions. Given that all the weakly shocked chondrites show evidence for inheritance of high temperatures from their initial formation conditions, and that these conditions resulted in tight-fitting chondrule aggregates ("cluster chondrite") that are obviously lithified (Metzler, 2012; Ruzicka et al., 2024), they must represent an early episode of lithification.

At the elevated temperatures of accretion, stickiness between colliding chondrules would be promoted by annealing between warm chondrules and by feldspathic glass in chondrules that acted in a rubbery fashion while above the glass transition temperature, resulting in chondrules that were not overly rigid and better able to dampen collisions occurring between them (Ruzicka et al., 2024; Seret & Libourel, 2025). We note that *the "bouncing barrier" and "meter barrier" in planetesimal formation could be overcome by one of several proposed nebular dynamical processes* (Morbidelli & Raymond, 2016, and references therein) *involving chondrule aggregates of the type that we infer for the first step in lithification*. Following accretion into planetesimals, the chondrule aggregates would have been susceptible to brecciation in later impacts to produce clasts with cluster chondrite texture, as often observed in ordinary chondrites (Metzler, 2012), but they apparently began the lithification process for these chondrites.

In **Setting B**, lithification occurred in planetesimals that were globally warmed and undergoing thermal metamorphism, most probably by short-lived radioactive decay (e.g., Blackburn et al., 2017; Harrison & Grimm, 2010; Huss et al., 2006; Hutchison, 2004; Kleine et al., 2008; McSween Jr et al., 2002). These warm planetesimals were experiencing mostly low velocity impact collisions that would have helped prevent collisional disruption and would explain the low degree of shock deformation recorded by the silicates (Figure 9). The warm bodies would likely have been hotter in their centers and cooler at their margins owing to conductive heat transfer (the "onion shell model" resulting from short-lived radioactive decay). Cratering events on these bodies that did not result in collisional disruption would have fractured silicates and compressed materials in the crater floor and subfloor areas, fluidizing metal and troilite, and affecting a range of metamorphic grades or petrographic types depending on depth of cratering, the interior temperatures at the time of cratering, and the previous impact history that could have scrambled materials from different depths. These floor and subfloor

19455100, 0, Downloaded from https://onlinelibrary.wiley.com/doi/10.1111/maps.70246 by ALEX RUZICKA , Wiley Online Library on [09/11/2026]. See the Terms and Conditions (https://onlinelibrary.wiley.com/terms-and-conditions) on Wiley Online Library for rules of use; OA articles are governed by the applicable Creative Commons License

areas could be where most of the weakly shocked chondrites (Saratov, Bjurböle, NWA 7298 Lithology A and C) formed (Figure 9).

A fallback origin is also possible for Baszkówka and Lithology B in NWA 7298. For Baszkówka, the data can be best explained by an ejecta deposition or re-accretion model (Figure 9), with re-deposited ejecta becoming buried somewhat to help keep materials warm for a time. Lithology B of NWA 7298 either could have formed in crater deposits beneath a more energetic impact on an intact body, or as highly shocked ejecta that was lofted above the planetesimal and redeposited on the surface (Figure 9). Here, following further cratering events, Lithology B could be incorporated as a clast in the NWA 7298 breccia, in accordance with the model presented by Friedrich, Weisberg, et al. (2014).

In **Setting C**, lithification occurred in planetesimals that were cold, after the fading of metamorphic heat. These planetesimals experienced higher velocity collisions, possibly with smaller impactors to help inhibit collisional disruption. Crater floor and subfloor areas for these energetic cratering events could be where the strongly shocked chondrites (NWA 11351, Alfianello, NWA 8709, NWA 4860) formed (Figure 9). Cratering events would have resulted in much plastic deformation of silicates, continued fluidization of metal and troilite, and more-or-less melting. Materials proximal to the collision contact point would be the most strongly deformed and heated, whereas material farther away would be less affected, giving a range of shock intensities (Stöffler et al., 2018). As ambient temperatures were low, the strongly shocked lithologies all cooled relatively rapidly after shock. The slightly higher porosity of Alfianello compared to other strongly shocked samples suggests it was not as strongly compressed, perhaps indicating it formed mainly as fallback ejecta (Figure 9).

Thus, *ordinary chondrites and their chondrules could have been lithified in different ways and times, but evidently always involving a combination of collisions and heat*. This includes low-velocity collisions between warm chondrules during accretion (Setting A), low-velocity collisional shocks on warm parent bodies (Setting B), and high-velocity collisional shocks on cold parent bodies (Setting C) (Figure 9).

However, collisions can also disrupt. Planetary regoliths are good examples of materials that dominantly experienced fragmentation and comminution by repeated impacts (Spray, 2016). Surficial regoliths are certainly present on asteroidal bodies of different sizes (e.g., Clark et al., 2002; Denevi et al., 2016; Miyamoto et al., 2007). Furthermore, for low-gravity bodies, rubble piles produced by collisional disruption and re-accretion should be common (Beitz et al., 2016; Hartmann, 1979; Michel et al., 2001; Scheeres et al., 2002). Rubble piles can be considered as composed entirely of regolith (Walsh, 2018) and are the ultimate of an unconsolidated body. Small asteroids imaged by spacecraft often appear to be rubble piles (e.g., Robin et al., 2024; Walsh, 2018). Although all asteroids less than about 10 km across are probably rubble piles (Walsh, 2018), even the presumed larger parent bodies of ordinary chondrites appear to have formed as rubble piles early, while they were still warm and undergoing thermal metamorphism (Blackburn et al., 2017; Grimm, 1985; Rubin, 2026; Taylor et al., 1987). However, with continued metamorphism, these reaccreted bodies could have become lithified, although subject to later disruption again. Asteroidal regoliths and rubble piles will contain a mix of lithified and non-lithified material, including boulders that are obviously lithified (e.g., Robin et al., 2024).

For each of the three proposed lithification settings, collisional processes resulting in lithification could have been associated with fragmentation that would oppose lithification. In Setting A, cluster chondrite textures produced by warm chondrule accretion (Metzler, 2012; Ruzicka et al., 2024; Seret & Libourel, 2025) are always present as clasts (Metzler, 2012). This suggests widespread fragmentation following or associated with lithification. Similarly, colliding chondrules may have fragmented or bounced if collisional velocities were too high (Güttler et al., 2010; Zsom et al., 2011) or if they were insufficiently warm. In Setting B, all the weakly shocked chondrites are relatively porous with most porosity in interchondrule (or "matrix") areas and all show evidence for fragmentation that especially affected silicates. Although all were lithified by a combination of compaction and heat (weakly shocked Bjurböle was arguably barely lithified), these materials likely coexisted with unconsolidated regolith that experienced more fragmentation, less compaction, or less annealing. In Setting C, fragmentation is less evident for the strongly shocked chondrites because they were overprinted by strong deformation effects. However, prior to shock, these chondrites could have resembled weakly shocked chondrites by being more fractured and more porous. For instance, NWA 8709 could have had porous matrix and an overall bulk porosity of ~23% prior to melt breccia formation (Ruzicka et al., 2020), similar to the most porous weakly shocked chondrites in this study (~19%–20%).

These considerations suggest that collisions on ordinary chondrite parent bodies produced both lithified rocks and unconsolidated debris, and that multiple collisions could have converted unconsolidated to lithified material, or lithified to unconsolidated material, during cycles of repeated impacts. Lithification and fragmentation of ordinary chondrite source materials were likely coeval and alternating processes in collisional

19455100, 0, Downloaded from https://onlinelibrary.wiley.com/doi/10.1111/maps.70246 by ALEX RUZICKA , Wiley Online Library on [09/11/2026]. See the Terms and Conditions (https://onlinelibrary.wiley.com/terms-and-conditions) on Wiley Online Library for rules of use; OA articles are governed by the applicable Creative Commons License

processing. But only the lithified rocks were sampled as meteorites.

Fluidization and Metal–Silicate Textures

A widely observed textural feature in the samples of this study is what is described as the fluidization of metal, whereby metal has behaved in a fluid-like state to partly or wholly envelop silicate grains or chondrules, or to form vein-like features. This texture occurs in lithologies with a wide range in shock stages (WSS = 1.49–5.74, CSS = S1-S6). Only Baszkówka lacks these textures in the samples studied. The evidence is compelling that such fluidization occurred largely in the solid state and in situ, as metal grains are internally deformed and are especially deformed against their edges with silicates. Seemingly, the only way that the grains could be explained by melting is to posit deformation in a second event after melting and solidification, for which there is no other evidence. We might expect evidence for a late shock such as found in Bjurböle in all weakly shocked chondrites, but do not find this (see "Thermomechanical Histories for Different Lithologies" section). It is much more likely that the grains were fluidized and deformed in the same event.

It is well recognized that materials (and especially metals) can flow like liquids even when not melted during impact events (Bourne, 2014, 2025; Signetti & Heine, 2021, 2022). Such "hydrodynamic flow" is characteristic for materials in a stronger shock regime when the shear strength of the material is exceeded (Bourne, 2014, 2025; Bourne & Bourne, 2022). For bcc Fe-metal, the transition to complete hydrodynamic flow occurs at shock pressures of ~13 GPa (Bourne, 2014), which is higher than the ~2.9–6.1 GPa pressure estimated for weakly shocked chondrites that show good evidence for metal and troilite fluidization. However, some fluidization is expected above the HEL in weaker shock regimes, too, owing to heterogeneous deformation that is characteristic of such weaker shocks (Bourne, 2014; Bourne & Bourne, 2022; Signetti & Heine, 2021, 2022). That bcc metal grains in weakly shocked chondrites were indeed deformed in a weak shock regime, and not in a strong shock regime dominated by hydrodynamic flow, is suggested by heterogeneous deformation features in the grains, including intragranular deformation and deformation twins. The propensity for materials to undergo hydrodynamic flow is linked to their HEL values, with pure hydrodynamic flow beginning at pressures roughly 10 times that of the HEL (Bourne, 2014). Thus, metal and troilite with their lower HEL values will be more easily fluidized than those with higher HEL values such as olivine.

Other meteorite types with apparently fluidic metal and metal–silicate textures similar to those reported here have been interpreted as evidence of metallic melt produced during shock deformation. *The data presented here provide a caution that fluidized metal may not always be a signature of melting*. Prominent examples of bcc metal fluidization textures that have been attributed to melting include a variety of silicate-bearing iron meteorites of different types (Ruzicka, 2014, and references therein; also Kirby, 2024); and many EL and EH enstatite chondrites that have been interpreted as melt breccias largely on the basis of textures (Rubin & Scott, 1997; van Niekerk & Keil, 2011, and references therein). To produce Fe-metal melt by shock would require high pressures (~218 GPa; Bourne, 2025), although some eutectic melting of metal can occur at lower pressures (Moreau et al., 2017, 2018). If the metal–silicate textures can be formed by solid-state fluidization processes during weak shocks instead of by melting, it would lead to significant re-interpretations for the origins of the rocks. In this study, elevated temperatures during shock may have facilitated fluidization of metal at low shock stages, but elevated temperatures were not necessary at high shock stages, so the exact role of ambient temperature to enable fluidization in these and other cases is poorly known. In any case, it could be fruitful to re-evaluate the evidence for the melting of metal in many meteorites considering the data presented here.

CONCLUSION

Studies of 11 lithologies in eight H, L, and LL chondrites span a large range in porosity (~2.6%–20.4%), metal 3-D shape preferred orientation (SPO, C ~ 0.12–1.14), and shock stage (CSS=S1–S6, WSS = 1.07–5.74), with good evidence that progressive shock compaction decreased porosity and increased metal SPO.

In these chondrites, the value of average olivine grain orientation spread ($GOS_{d>50}$ in degrees) corresponds roughly to the weighted shock stage, and both (together with olivine $GOS_{d15\text{-}50}$) are good measures of overall shock intensity, supporting and extending previous conclusions (Ruzicka et al., 2024; Ruzicka & Hugo, 2018). GOS is probably related to the amount of shear strain experienced by minerals, up to the point of recrystallization or melting. For most chondrites, average $GOS_{d15\text{-}50}$ values increase in the sequence olivine < troilite < bcc metal, and together with differences in fracturing and texture, indicate differences in mineral deformation response. In weakly shocked chondrites (Baszkówka, Bjurböle, Saratov, and NWA 7298 Lithology A and C), silicates were dominantly fractured and have lower GOS values, whereas metal and troilite were largely fluidized and have higher GOS values. These weakly shocked chondrites probably experienced stresses close to the

19455100, 0, Downloaded from https://onlinelibrary.wiley.com/doi/10.1111/maps.70246 by ALEX RUZICKA , Wiley Online Library on [09/11/2026]. See the Terms and Conditions (https://onlinelibrary.wiley.com/terms-and-conditions) on Wiley Online Library for rules of use; OA articles are governed by the applicable Creative Commons License

Hugoniot Elastic Limit of constituent minerals (~4–7 GPa) during impact. In strongly shocked chondrites (NWA 7298 Lithology B, NWA 11315 Lithology A and B, Alfianello, NWA 8709, NWA 4860), stresses were higher (>7 GPa) during impact, olivine was more strained, and metal and troilite experienced dynamic recovery keeping their GOS values relatively uniform. The data imply that mean shock pressures for weakly shocked chondrites (CSS=S1-S2, WSS = 1.07–1.79) were ~2.9–6.1 GPa and mean shock pressures for strongly shocked chondrites (CSS=S4-S6, WSS = 3.76–5.74) were >6.1 GPa.

The weakly shocked chondrites probably were affected by impacts occurring on warm parent bodies that were undergoing thermal metamorphism. Evidence based on textures, recrystallization, and recovery features and GOS skewness-grain size data suggest: (1) minor recrystallization in silicates for Baszkówka and Bjurböle and for metal in NWA 7298 Lithology A and C, best attributed to a static recrystallization process caused by elevated temperatures after shock; (2) extensive recrystallization of troilite in NWA 7298 Lithology A and B, best attributed to elevated pre-shock temperatures; (3) recovery on a small scale (≤5 μm) for Baszkówka and Saratov, consistent with some annealing after shock; and (4) evidence in Bjurböle for extensive annealing early, probably caused by burial in a warm parent body that had experienced some weak shocks, along with a later weak shock event that caused fracturing and brought Bjurböle into a cooler near-surface environment. Baszkówka probably formed in warm ejecta that was deposited near the surface of the body. All the weakly shocked chondrites have olivine with elevated $R_{2\text{-}10}$ values suggestive of deformation at elevated temperatures, but these $R_{2\text{-}10}$ values were probably inherited from earlier nebular processes (e.g., warm accretion), consistent with Ruzicka et al. (2024).

Most strongly shocked chondrites (NWA 11351 Lithology A and B, Alfianello, NWA 8709, NWA 4860) were affected by impacts occurring on cool parent bodies although Lithology B of NWA 7298 is best explained by a strong impact on a warm body. For the chondrites involving cool protoliths, a maximum average shock reheating temperature for olivine of $T_{deform} \sim 775$–800 °C is inferred. For NWA 7298 Lithology B, a high T_{deform} value of ~997 °C is best explained by a superposition of shock reheating and elevated pre-shock temperature. All the strongly shocked chondrites experienced some shock melting, and all appear to have cooled relatively quickly after shock. For the strongest shocks experienced by the melt breccias NWA 8709 and NWA 4860, considerable melting occurred within matrix, olivine experienced significant recrystallization, and troilite largely melted. In NWA 4860, shock-generated vapor created vugs in which various minerals (including troilite) condensed. In NWA 8709, an interplay between melting and recrystallization was transforming this type 3 chondrite into a melt rock.

Lithification and fragmentation of ordinary chondrite source materials were likely coeval and sequential processes in collisional processing. Three lithification settings are proposed: (1) Setting A, likely affecting all ordinary chondrites, involving the initial agglomeration of warm chondrule aggregates during low-velocity collisions; (2) Setting B, associated with impacts on warm parent bodies, including crater floor and subfloor areas (displaced zone) (Saratov, Bjurböle, NWA 7298 Lithology A and C), with Baszkówka and possibly NWA 7298 Lithology B forming as redeposited ejecta from impact events on warm bodies; and (3) Setting C, associated with higher velocity collisions on cold parent bodies, including crater floor and subfloor areas (NWA 11315 all lithologies, NWA 8709, NWA 4860), with Alfianello possibly forming as redeposited ejecta. For Setting A, warm temperatures and "rubbery" behavior of chondrules, together with low velocities, likely helped overcome the "bouncing barrier" between colliding chondrules. For Setting B, warm materials and the fluidization of metal and troilite by impact were probably key factors in enabling lithification. For Setting C, strong shock compression and heating effects that included melting were probably most important for lithification.

Fluidization of metal occurred even in the solid state during low-intensity shock events. Besides being of possible importance for lithification, this suggests caution in the interpretation of metal–silicate textures in meteorites as a signature for melting of metal.

Conflict of Interest Statement—The authors declare that they have no known competing financial interests or personal relationships that could have appeared to influence the work reported in this paper.

Acknowledgments—This work was supported by NASA grant 80NSSC19K0517. The authors thank Dr. Alan Rubin and an anonymous reviewer for comments that helped improve the quality of this manuscript, and Dr. John Spray for comments and Dr. Spray and Dr. Timothy Jull for editorial handling.

Data Availability Statement—Data are available through PDXScholar at https://pdxscholar.library.pdx.edu/geology_data/9/ (https://doi.org/10.15760/geology-data.09) (Ruzicka et al., 2026).

Editorial Handling—John G. Spray

19455100, 0, Downloaded from https://onlinelibrary.wiley.com/doi/10.1111/maps.70246 by ALEX RUZICKA , Wiley Online Library on [09/11/2026]. See the Terms and Conditions (https://onlinelibrary.wiley.com/terms-and-conditions) on Wiley Online Library for rules of use; OA articles are governed by the applicable Creative Commons License

REFERENCES

Ayad, A., Allain-Bonasso, N., Rouag, N., and Wagner, F. 2012. Grain Orientation Spread Values in IF Steels after Plastic Deformation and Recrystallization. In *Materials Science Forum*, vol. 702, 269–272. Trans Tech Publications Ltd.

Beitz, E., Blum, J., Parisi, M. G., and Trigo-Rodriguez, J. 2016. The Collisional Evolution of Undifferentiated Asteroids and the Formation of Chondritic Meteoroids. *Astrophysical Journal* 824: 12.

Beitz, E., Güttler, C., Nakamura, A. M., Tsuchiyama, A., and Blum, J. 2013. Experiments on the Consolidation of Chondrites and the Formation of Dense Rims around Chondrules. *Icarus* 225: 558–569.

Bennett, M. E., III, and McSween, H. Y. 1996. Shock Features in Iron-Nickel Metal and Troilite of L-Group Ordinary Chondrites. *Meteoritics & Planetary Science* 31: 255–264.

Bischoff, A., Rubin, A. E., Keil, K., and Stöffler, D. 1983. Lithification of Gas-Rich Chondrite Regolith Breccias by Grain Boundary and Localized Shock Melting. *Earth and Planetary Science Letters* 66: 1–10.

Bischoff, A., Schleiting, M., and Patzek, M. 2019. Shock Stage Distribution of 2280 Ordinary Chondrites—Can Bulk Chondrites with a Shock Stage of S6 Exist as Individual Rocks? *Meteoritics & Planetary Science* 54: 2189–2202.

Blackburn, T., Alexander, C. M. D., Carlson, R., and Elkins-Tanton, L. T. 2017. The Accretion and Impact History of the Ordinary Chondrite Parent Bodies. *Geochimica et Cosmochimica Acta* 200: 201–217.

Bland, P. A., Collins, G. S., Davison, T. M., Abreu, N. M., Ciesla, F. J., Muxworthy, A. R., and Moore, J. 2014. Pressure–Temperature Evolution of Primordial Solar System Solids during Impact-Induced Compaction. *Nature Communications* 5: 5451.

Bland, P. A., Howard, L. E., Prior, D. J., Wheeler, J., Hough, R. M., and Dyl, K. A. 2011. Earliest Rock Fabric Formed in the Solar System Preserved in a Chondrule Rim. *Nature Geoscience* 4: 244–47.

Bouquerel, J., Schayes, C., and Vogt, J. B. 2021. Experimental Mesoscopic Investigation of the Local Cyclic Plasticity of a Non-oriented Electrical Steel. *Materials Science and Engineering A* 820: 141454.

Bourne, N. K. 2014. The Threshold for Hydrodynamic Behaviour in Solids under Extreme Compression. *Journal of Applied Physics* 116: 093505. https://doi.org/10.1063/1.4894138.

Bourne, N. K. 2025. A Limit to Strong Shock Behavior in the Dynamic Response of Matter at Pressure. *Journal of Applied Physics* 137: 205906. https://doi.org/10.1063/5.0249977.

Bourne, N. K., and Bourne, F. L. 2022. On the Transition from Weak to Strong Shock Response. *Journal of Applied Physics* 131: 145901. https://doi.org/10.1063/5.0084553.

Brewer, L. N., Field, D. P., and Merriman, C. C. 2009. Mapping and Assessing Plastic Deformation Using EBSD. In *Electron Backscatter Diffraction in Materials Science*, edited by A. J. Schwartz, M. Kumar, B. L. Adams, and D. P. Field, 251–262. Boston, MA: Springer.

Cheng, Y., Song, C., Tan, Y., Yue, S., Li, G., Qiu, Y., Xu, T., Liu, Y., Gao, F., and Yu, Q. 2021. Theoretical Calculation Method for the Hugoniot Elastic Limit of Hard Rock Based on Ideal Elastoplastic Model. *Shock and Vibration*: 6677077.

Christensen, N. I. 1996. Poisson's Ratio and Crustal Seismology. *Journal of Geophysical Research: Solid Earth* 101(B2): 3139–56.

Ciesla, F. J., Davison, T. M., Collins, G. S., and O'Brien, D. P. 2013. Thermal Consequences of Impacts in the Early Solar System. *Meteoritics & Planetary Science* 48: 2559–76.

Clark, B. E., Hapke, B., Pieters, C., and Britt, D. 2002. Asteroid Space Weathering and Regolith Evolution. In *Asteroids III*, edited by W. F. Bottke, Jr., A. Cellino, P. Paolicchi, and R. P. Binzel, 595–99. Tucson: University of Arizona Press.

Collins, G. S., Housen, K. R., Jutzi, M., and Nakamura, A. M. 2019. Planetary Impact Processes in Porous Materials. In *Shock Phenomena in Granular and Porous Materials*, 103–136. Cham: Springer International Publishing.

Consolmagno, S. J. G. J., and Britt, D. T. 2004. Meteoritical Evidence and Constraints on Asteroid Impacts and Disruption. *Planetary and Space Science* 52: 1119–28.

Consolmagno, S. J. G. J., Britt, D. T., and Stoll, C. P. 1998. The Porosities of Ordinary Chondrites: Models and Interpretation. *Meteoritics & Planetary Science* 33: 1221–29.

Denevi, B. W., Beck, A. W., Coman, E. I., Thomson, B. J., Ammannito, E., Blewett, D. T., Sunshine, J. M., et al. 2016. Global Variations in Regolith Properties on Asteroid Vesta from Dawn's Low-Altitude Mapping Orbit. *Meteoritics & Planetary Science* 51: 2366–86.

Druiventak, A., Matysiak, A., Renner, J., and Trepmann, C. A. 2012. Kick-and-Cook Experiments on Peridotite: Simulating Coseismic Deformation and Post-Seismic Creep. *Terra Nova* 24: 62–69.

Forman, L. V., Bland, P. A., Timms, N. E., Collins, G. S., Davison, T. M., Ciesla, F. J., Benedix, G. K., et al. 2016. Hidden Secrets of Deformation: Impact-Induced Compaction within a CV Chondrite. *Earth and Planetary Science Letters* 452: 133–145.

Friedrich, J. M., Macke, R. J., Wignarajah, D. P., Rivers, M. L., Britt, D. T., and Ebel, D. S. 2008. Pore Size Distribution in an Uncompacted Equilibrated Ordinary Chondrite. *Planetary and Space Science* 56: 895–900.

Friedrich, J. M., Rubin, A. E., Beard, S. P., Swindle, T. D., Isachsen, C. E., Rivers, M. L., and Macke, R. J. 2014. Ancient Porosity Preserved in Ordinary Chondrites: Examining Shock and Compaction on Young Asteroids. *Meteoritics & Planetary Science* 49: 1214–31.

Friedrich, J. M., Ruzicka, A., Macke, R. J., Thostenson, J. O., Rudolph, R. A., Rivers, M. L., and Ebel, D. S. 2017. Relationships among Physical Properties as Indicators of High Temperature Deformation or Post-Shock Thermal Annealing in Ordinary Chondrites. *Geochimica et Cosmochimica Acta* 203: 157–174.

Friedrich, J. M., Weisberg, M. K., and Rivers, M. L. 2014. Multiple Impact Events Recorded in the NWA 7298 H Chondrite Breccia and the Dynamical Evolution of an Ordinary Chondrite Asteroid. *Earth and Planetary Science Letters* 394: 13–19.

Friedrich, J. M., Wignarajah, D. P., Chaudhary, S., Rivers, M. L., Nehru, C. E., and Ebel, D. S. 2008. Three-Dimensional Petrography of Metal Phases in Equilibrated L Chondrites—Effects of Shock Loading and Dynamic Compaction. *Earth and Planetary Science Letters* 275: 172–180.

19455100, 0, Downloaded from https://onlinelibrary.wiley.com/doi/10.1111/maps.70246 by ALEX RUZICKA , Wiley Online Library on [09/11/2026]. See the Terms and Conditions (https://onlinelibrary.wiley.com/terms-and-conditions) on Wiley Online Library for rules of use; OA articles are governed by the applicable Creative Commons License

Fritz, J., Greshake, A., and Fernandes, V. A. 2017. Revising the Shock Classification of Meteorites. *Meteoritics & Planetary Science* 52: 1216–32.

Fruland, R. M. 1975. *Impact-Generated Volatile Movement and Redistribution in the Rose City Meteorite*. MS Thesis. Houston, Texas: University of Houston. DSPACE, https://uh-ir.tdl.org, accessed February 5, 2026.

Fujiyama, K., Kimachi, H., Watanabe, Y., Hijikuro, K., and Tsuboi, T. 2011. The Concept of "EBSD Strain Analysis" and its Application to Creep and Creep-Fatigue Damage Assessment of Ferritic and Austenitic Heat Resistant Steels. *Strength, Fracture and Complexity* 7: 123–135.

Gattacceca, J., Rochette, P., Denise, M., Consolmagno, G., and Folco, L. 2005. An Impact Origin for the Foliation of Chondrites. *Earth and Planetary Science Letters* 234: 351–368.

Goudy, S. P., Telus, M., and Chapman, B. 2023. Evidence for Multiple Early Impacts on the H Chondrite Parent Body from Electron Backscatter Diffraction Analysis. *Meteoritics & Planetary Science* 58: 501–515.

Grimm, R. E. 1985. Penecontemporaneous Metamorphism, Fragmentation, and Reassembly of Ordinary Chondrite Parent Bodies. *Journal of Geophysical Research - Solid Earth* 90(B2): 2022–28.

Gueguen, Y., and Nicolas, A. 1980. Deformation of Mantle Rocks. *Annual Review of Earth and Planetary Sciences* 8: 119–144.

Guignard, J., and Toplis, M. J. 2015. Textural Properties of Iron-Rich Phases in H Ordinary Chondrites and Quantitative Links to the Degree of Thermal Metamorphism. *Geochimica et Cosmochimica Acta* 149: 46–63.

Güttler, C., Blum, J., Zsom, A., Ormel, C. W., and Dullemond, C. P. 2010. The Outcome of Protoplanetary Dust Growth: Pebbles, Boulders, or Planetesimals?-I. Mapping the Zoo of Laboratory Collision Experiments. *Astronomy & Astrophysics* 513: A56.

Hanna, R. D., Ketcham, R. A., Zolensky, M., and Behr, W. M. 2015. Impact-Induced Brittle Deformation, Porosity Loss, and Aqueous Alteration in the Murchison CM Chondrite. *Geochimica et Cosmochimica Acta* 171: 256–282.

Harrison, K. P., and Grimm, R. E. 2010. Thermal Constraints on the Early History of the H-Chondrite Parent Body Reconsidered. *Geochimica et Cosmochimica Acta* 74: 5410–23.

Hartmann, W. K. 1979. Diverse Puzzling Asteroids and a Possible Unified Explanation. In *Asteroids*, edited by T. Gehrels, 466–479. Tucson: University of Arizona Press.

Holsapple, K., Giblin, I., Housen, K., Nakamura, A., and Ryan, E. 2002. Asteroid Impacts: Laboratory Experiments and Scaling Laws. In *Asteroids III*, edited by W. F. Bottke, Jr., A. Cellino, P. Paolicchi, and R. P. Binzel, 443–462. Tucson: University of Arizona Press.

Hörz, F., Cintala, M. J., See, T. H., and Le, L. 2005. Shock Melting of Ordinary Chondrite Powders and Implications for Asteroidal Regoliths. *Meteoritics & Planetary Science* 40: 1329–46.

Hugo, R. C., Ruzicka, A. M., and Rubin, A. E. 2020. Mesoscale and Microscale Shock Effects in the LL6 S4 Chondrites Saint-Séverin and Elbert: A Tale of Two Breccias. *Meteoritics & Planetary Science* 55: 1418–38.

Huss, G. R., Rubin, A. E., and Grossman, J. N. 2006. Thermal Metamorphism in Chondrites. In *Meteorites and the Early Solar System II*, edited by D. S. Lauretta, and H. Y. McSween, Jr., 567–586. Tucson: University of Arizona Press.

Hutchison, R. 2004. *Meteorites: A Petrologic, Chemical and Isotopic Synthesis*. Cambridge: Cambridge University Press.

Jamsja, N., and Ruzicka, A. 2010. Shock and Thermal History of Northwest Africa 4859, an Annealed Impact-Melt Breccia of LL Chondrite Parentage Containing Unusual Igneous Features and Pentlandite. *Meteoritics & Planetary Science* 45: 828–849.

Kang, J. Y., Bacroix, B., Réglé, H., Oh, K. H., and Lee, H. C. 2007. Effect of Deformation Mode and Grain Orientation on Misorientation Development in a Body-Centered Cubic Steel. *Acta Materialia* 55: 4935–46.

Karato, S. I., Jung, H., Katayama, I., and Skemer, P. 2008. Geodynamic Significance of Seismic Anisotropy of the Upper Mantle: New Insights from Laboratory Studies. *Annual Review of Earth and Planetary Sciences* 36: 59–95.

Kieffer, S. W. 1975. From Regolith to Rock by Shock. *The Moon* 13: 301–320.

Kirby, R. S. 2024. *Metal on the Surface of Asteroids: Geochemistry, Petrogenesis and Thermal History of IIE Iron Meteorites and their Relationship to Ordinary Chondrites*. Ph.D. Dissertation, Canberra: Australian National University. Proquest Dissertations and Theses, Number 31855570.

Kleine, T., Touboul, M., Van Orman, J. A., Bourdon, B., Maden, C., Mezger, K., and Halliday, A. N. 2008. Hf–W Thermochronometry: Closure Temperature and Constraints on the Accretion and Cooling History of the H Chondrite Parent Body. *Earth and Planetary Science Letters* 270: 106–118.

Krzesińska, A., Gattacceca, J., Friedrich, J. M., and Rochette, P. 2015. Impact-Related Noncoaxial Deformation in the Pułtusk H Chondrite Inferred from Petrofabric Analysis. *Meteoritics & Planetary Science* 50: 401–417.

Krzesińska, A. M., and Almeida, N. V. 2019. Evidence of Shock-Induced Vaporization of Matrix to Form Porosity in Baszkówka, a Porous L5 Chondrite. *Meteoritics & Planetary Science* 54: 54–71.

Kunz, J., Falter, M., and Jessberger, E. K. 1997. Shocked Meteorites: Argon-40-Argon-39 Evidence for Multiple Impacts. *Meteoritics & Planetary Science* 32: 647–670.

Lagerlöf, K. P. D. 1993. On Deformation Twinning in Bcc Metals. *Acta Metalllurgica et Materialia* 41: 2143–51.

Lloyd, G. E., Farmer, A. B., and Mainprice, D. 1997. Misorientation Analysis and the Formation and Orientation of Subgrain and Grain Boundaries. *Tectonophysics* 279: 55–78.

Lubliner, J. 2006. *Plasticity Theory*, Revised ed. Berkeley: University of California. https://www.scribd.com/document/21551320/Plasticity-Theory-Jacob-Lubliner, accessed February 26, 2026.

Luo, Y., Chen, H., Beard, S., Zeng, X., Hu, S., Du, Z., Jin, L., Liu, J., Li, S., and Zhang, X. 2024. EBSD Analysis of Iron-Nickel Metal in L Type Ordinary Chondrites: 1. The Microstructural Shock Signatures. *Journal of Geophysical Research, Planets* 129: e2023JE007938.

Macente, A., Daly, L., Griffin, S., Gritsevich, M., Moilanen, J., Einsle, J. F., Trimby, P., Mulcahy, C., Moffat, J., and Ruzicka, A. M. 2025. The Petrology of the Ozerki Meteorite Constrained by Electron Backscatter Diffraction and X-Ray Computed Tomography. *Meteoritics & Planetary Science* 60: 1095–1118.

Macke, R. J. 2010. *Survey of Meteorite Physical Properties Density, Porosity and Magnetic Susceptibility*. Ph.D.

19455100, 0, Downloaded from https://onlinelibrary.wiley.com/doi/10.1111/maps.70246 by ALEX RUZICKA , Wiley Online Library on [09/11/2026]. See the Terms and Conditions (https://onlinelibrary.wiley.com/terms-and-conditions) on Wiley Online Library for rules of use; OA articles are governed by the applicable Creative Commons License

Dissertation, Orlando, Florida: Univ. Central Florida. STARS 1638. https://stars.library.ucf.edu/etd/1638.
Macke, R. J., Kent, J. J., Kiefer, W. S., and Britt, D. T. 2015. 3D-Laser-Scanning Technique Applied to Bulk Density Measurements of Apollo Lunar Samples. *Lunar Planetary Science Conference XLVI*, abstract #1716.
Maki, T. 2012. Morphology and Substructure of Martensite in Steels. In *Phase Transformations in Steels*, edited by E. Pereloma, and D. V. Edmonds, vol. 2, 34–58. Cambridge: Woodhead Publishing. https://doi.org/10.1533/9780857096111.1.34.
Mao, G., Cayron, C., Mao, X., Cao, R., Logé, R., and Chen, J. 2018. Morphological and Crystallographic Characteristics of α Structure in a Low-Carbon Iron–Nickel Alloy. *Crystals* 8: 468.
MBD. 2026. *Meteoritical Bulletin Database*. https://www.lpi.usra.edu/meteor/, accessed January 15, 2026.
McSween, H. Y., Jr., Ghosh, A., Grimm, R. E., Wilson, L., and Young, E. D. 2002. Thermal Evolution Models of Asteroids. In *Asteroids III*, edited by W. F. Bottke, Jr., A. Cellino, P. Paolicchi, and R. P. Binzel, 559–572. Tucson: University of Arizona Press.
Melosh, H. J. 1989. *Impact Cratering: A Geologic Process*. Oxford Monographs on Geology and Geophysics No. 11. Oxford: Clarendon Press.
Melosh, H. J., and Ryan, E. V. 1997. Asteroids: Shattered but Not Dispersed. *Icarus* 129: 562–64.
Metzler, K. 2012. Ultrarapid Chondrite Formation by Hot Chondrule Accretion? Evidence from Unequilibrated Ordinary Chondrites. *Meteoritics & Planetary Science* 47: 2193–2217.
Michel, P., Benz, W., Tanga, P., and Richardson, D. C. 2001. Collisions and Gravitational Reaccumulation: Forming Asteroid Families and Satellites. *Science* 294: 1696–1700.
Miyamoto, H., Yano, H., Scheeres, D. J., Abe, S., Barnouin-Jha, O., Cheng, A. F., Demura, H., et al. 2007. Regolith Migration and Sorting on Asteroid Itokawa. *Science* 316: 1011–14.
Morbidelli, A., and Raymond, S. N. 2016. Challenges in Planet Formation. *Journal of Geophysical Research, Planets* 121: 1962–80.
Moreau, J., Kohout, T., and Wünnemann, K. 2017. Shock-Darkening in Ordinary Chondrites: Determination of the Pressure-Temperature Conditions by Shock Physics Mesoscale Modeling. *Meteoritics & Planetary Science* 52: 2375–90.
Moreau, J. G., Kohout, T., and Wünnemann, K. 2018. Melting Efficiency of Troilite-Iron Assemblages in Shock-Darkening: Insight from Numerical Modeling. *Physics of the Earth and Planetary Interiors* 282: 25–38.
Mushnikov, N. V., Popov, A. G., Gaviko, V. S., Protasov, A. V., Kleinerman, N. M., Golovnya, O. A., and Naumov, S. P. 2022. Peculiarities of Phase Diagram of Fe-Ni System at Ni Concentrations 0–20 at.%. *Acta Materialia* 240: 118330.
Nakamura, T., Tomeoka, K., Takaoka, N., Sekine, T., and Takeda, H. 2000. Impact-Induced Textural Changes of CV Carbonaceous Chondrites: Experimental Reproduction. *Icarus* 146: 289–300.
Noonan, J. W., Reddy, V., Harris, W. M., Bottke, W. F., Sanchez, J. A., Furfaro, R., Brown, Z., et al. 2019. Search for the H Chondrite Parent Body among the Three Largest S-Type Asteroids: (3) Juno,(7) Iris, and (25) Phocaea. *Astronomical Journal* 158: 213.
Obata, M., Mashimo, T., Ando, J., Chen, L., Kawai, N., Liu, X., and Yamamoto, T. 2023. High-Pressure Shock Compression of Olivine: Dynamic Pulverization and Frictional Melting. *Physics of the Earth and Planetary Interiors* 338: 107009.
Ogilvie, P., Gibson, R. L., Reimold, W. U., Deutsch, A., and Hornemann, U. 2011. Experimental Investigation of Shock Metamorphic Effects in a Metapelitic Granulite: The Importance of Shock Impedance Contrast between Components. *Meteoritics & Planetary Science* 46: 1565–86.
Olsen, E. 1981. Vugs in Ordinary Chondrites. *Meteoritics* 16: 45–59.
Pardis, N., Ebrahimi, R., and Kim, H. S. 2017. Equivalent Strain at Large Shear Deformation: Theoretical, Numerical and Finite Element Analysis. *Journal of Applied Research & Technology* 15: 442–48.
Passchier, C. W., and Trouw, R. A. 2005. *Microtectonics*. Berlin Heidelberg: Springer.
Reisener, R. J., and Goldstein, J. I. 2003a. Ordinary Chondrite Metallography: Part 1. Fe-Ni Taenite Cooling Experiments. *Meteoritics & Planetary Science* 38: 1669–78.
Reisener, R. J., and Goldstein, J. I. 2003b. Ordinary Chondrite Metallography: Part 2. Formation of Zoned and Unzoned Metal Particles in Relatively Unshocked H, L, and LL Chondrites. *Meteoritics & Planetary Science* 38: 1679–96.
Robin, C. Q., Duchene, A., Murdoch, N., Vincent, J. B., Lucchetti, A., Pajola, M., Ernst, C. M., et al. 2024. Mechanical Properties of Rubble Pile Asteroids (Dimorphos, Itokawa, Ryugu, and Bennu) through Surface Boulder Morphological Analysis. *Nature Communications* 15: 6203.
Rubin, A. E. 2004. Postshock Annealing and Postannealing Shock in Equilibrated Ordinary Chondrites: Implications for the Thermal and Shock Histories of Chondritic Asteroids. *Geochimica et Cosmochimica Acta* 68: 673–689.
Rubin, A. E. 2025. Positive Correlation between Shock Stage and Petrologic Type in Ordinary Chondrites: Implications for the Internal Structures and Thermal Histories of Ordinary-Chondrite Parent Asteroids. *Meteoritics & Planetary Science* 60: 17–31.
Rubin, A. E. 2026. *Ordinary Chondrites: The Most Common Meteorites*. Cambridge: Cambridge University Press.
Rubin, A. E., and Scott, W. R. 1997. Abee and Related EH Chondrite Impact-Melt Breccias. *Geochimica et Cosmochimica Acta* 61: 425–435.
Ruzicka, A. 2014. Silicate-Bearing Iron Meteorites and their Implications for the Evolution of Asteroidal Parent Bodies. *Chemie der Erde-Geochemistry* 74: 3–48.
Ruzicka, A., Hugo, R., and Hutson, M. 2015. Deformation and Thermal Histories of Ordinary Chondrites: Evidence for Post-Deformation Annealing and Syn-Metamorphic Shock. *Geochimica et Cosmochimica Acta* 163: 219–233.
Ruzicka, A., Killgore, M., Mittlefehldt, D. W., and Fries, M. D. 2005. Portales Valley: Petrology of a Metallic-Melt Meteorite Breccia. *Meteoritics & Planetary Science* 40: 261–295.
Ruzicka, A. M., Friedrich, J. M., Hugo, R. C., Macke, R. J., Sheikh, D., and Hutson, M. 2026. Data From: Variably Shock-Compacted Chondrites: Deformation-Thermal Histories, Large Differences in Mineral Deformation Response, and Implications for Lithification. [Dataset].
Ruzicka, A. M., Friedrich, J. M., Hutson, M. L., Strasser, J. W., Macke, R. J., Rivers, M. L., Greenwood, R. C., Ziegler, K., and Pugh, R. N. 2020. Shock Compaction Heating and Collisional Processes in the Production of Type 3 Ordinary Chondrites: Lessons from the (Nearly)

19455100, 0, Downloaded from https://onlinelibrary.wiley.com/doi/10.1111/maps.70246 by ALEX RUZICKA , Wiley Online Library on [09/11/2026]. See the Terms and Conditions (https://onlinelibrary.wiley.com/terms-and-conditions) on Wiley Online Library for rules of use; OA articles are governed by the applicable Creative Commons License

Unique L3 Chondrite Melt Breccia Northwest Africa 8709. *Meteoritics & Planetary Science* 55: 2117–40.

Ruzicka, A. M., and Hugo, R. C. 2018. Electron Backscatter Diffraction (EBSD) Study of Seven Heavily Metamorphosed Chondrites: Deformation Systematics and Variations in Pre-Shock Temperature and Post-Shock Annealing. *Geochimica et Cosmochimica Acta* 234: 115–147.

Ruzicka, A. M., Hugo, R. C., Friedrich, J. M., and Ream, M. T. 2024. Accretion of Warm Chondrules in Weakly Metamorphosed Ordinary Chondrites and their Subsequent Reprocessing. *Geochimica et Cosmochimica Acta* 378: 1–35.

Scheeres, D. J., Durda, D. D., and Geissler, P. E. 2002. The Fate of Asteroid Ejecta. In *Asteroids III*, edited by W. F. Bottke, Jr., A. Cellino, P. Paolicchi, and R. P. Binzel, 527–544. Tucson: University of Arizona Press.

Schepker, K. L. 2014. *Complex Thermal Histories of L Melt Breccias NWA 5964 and NWA 6580*. M.S. Thesis, Portland, Oregon: Portland State University, PDXScholar, Paper 1835.

Schmitt, R. T. 2000. Shock Experiments with the H6 Chondrite Kernouvé: Pressure Calibration of Microscopic Shock Effects. *Meteoritics & Planetary Science* 35: 545–560.

Seret, A., and Libourel, G. 2025. Chondrites as Thermal and Mechanical Archives of Accretion Processes in the Solar Protoplanetary Disk. *Earth and Planetary Science Letters* 649: 119066.

Sharp, T. G., and DeCarli, P. S. 2006. Shock Effects in Meteorites. In *Meteorites and the Early Solar System II*, edited by D. S. Lauretta, and H. Y. McSween, Jr., 653–677. Tucson: University of Arizona Press.

Signetti, S., and Heine, A. 2021. Characterization of the Transition Regime between High-Velocity and Hypervelocity Impact: Thermal Effects and Energy Partitioning in Metals. *International Journal of Impact Engineering* 151: 103774.

Signetti, S., and Heine, A. 2022. Transition Regime between High-Velocity and Hypervelocity Impact in Metals–A Review of the Relevant Phenomena for Material Modeling in Ballistic Impact Studies. *International Journal of Impact Engineering* 167: 104213.

Singla, A., and Ray, A. 2022. Hugoniot Elastic Limit of Single-Crystal Tantalum at Normal and Elevated Temperatures Subjected to Extreme Strain Rates. *Physical Review B* 105: 064102.

Smith, J. A., Lacy, J. M., Lévesque, D., Monchalin, J. P., and Lord, M. 2016. Use of the Hugoniot Elastic Limit in Laser Shockwave Experiments to Relate Velocity Measurements. In *AIP Conference Proceedings*, vol. 1706, 080005. Melville, NY: AIP Publishing LLC.

Sneyd, D. S., McSween, H. Y., Jr., Sugiura, N., Strangway, D. W., and Nord, G. L., Jr. 1988. Origin of Petrofabrics and Magnetic Anisotropy in Ordinary Chondrites. *Meteoritics* 23: 139–149.

Soini, A. J., Kukkonen, I. T., Suhonen, H., Lukić, B., Kohout, T., and Luttinen, A. V. 2023. Investigation of the Porosity of L/LL4 Ordinary Chondrite Bjurböle Using Synchrotron Radiation Microtomography and Scanning Electron Microscopy: Implications for Parent Body Evolution. *Physics of the Earth and Planetary Interiors* 343: 107087.

Spray, J. G. 2016. Lithification Mechanisms for Planetary Regoliths: The Glue that Binds. *Annual Review of Earth and Planetary Sciences* 44: 139–174.

Stewart, S. T., and Leinhardt, Z. M. 2009. Velocity-Dependent Catastrophic Disruption Criteria for Planetesimals. *Astrophysical Journal* 691: L133–L137.

Stöffler, D., Bischoff, A., Buchwald, V., and Rubin, A. E. 1988. Shock Effects in Meteorites. In *Meteorites and the Early Solar System*, edited by J. F. Kerridge, and M. S. Mathews, 165–202. Tucson: University of Arizona Press.

Stöffler, D., Hamann, C., and Metzler, K. 2018. Shock Metamorphism of Planetary Silicate Rocks and Sediments: Proposal for an Updated Classification System. *Meteoritics & Planetary Science* 53: 5–49.

Stöffler, D., Hamann, C., and Metzler, K. 2019. Addendum to "Stöffler, D., Hamann, C., & Metzler, K. Shock Metamorphism of Planetary Silicate Rocks and Sediments: Proposal for an Updated Classification System. Meteoritics & Planetary Science, 53, 5-49, 2018". *Meteoritics & Planetary Science* 54: 946–49.

Stöffler, D., Keil, K., and Scott, E. R. D. 1991. Shock Metamorphism of Ordinary Chondrites. *Geochimica et Cosmochimica Acta* 55: 3845–67.

Swindle, T. D., Kring, D. A., and Weirich, J. R. 2014. 40Ar/39Ar Ages of Impacts Involving Ordinary Chondrite Meteorites. In *Advances in 40Ar/39Ar Dating: From Archaeology to Planetary Sciences*, edited by F. Jourdan, D. F. Mark, and C. Verati, 333–347. London: Geological Society Special Publications 378.

Syono, Y., Goto, T., Sato, J. I., and Takei, H. 1981. Shock Compression Measurements of Single-Crystal Forsterite in the Pressure Range 15–93 GPa. *Journal of Geophysical Research - Solid Earth* 86(B7): 6181–86.

Taylor, G. J., Maggiore, P., Scott, E. R., Rubin, A. E., and Keil, K. 1987. Original Structures, and Fragmentation and Reassembly Histories of Asteroids: Evidence from Meteorites. *Icarus* 69: 1–13.

Thomas, S. A., Hawkins, M. C., Matthes, M. K., Gray, G. T., and Hixson, R. S. 2018. Dynamic Strength Properties and Alpha-Phase Shock Hugoniot of Iron and Steel. *Journal of Applied Physics* 123: 175902.

Tomkins, A. G. 2009. What Metal-Troilite Textures Can Tell us about Post-Impact Metamorphism in Chondrite Meteorites. *Meteoritics & Planetary Science* 44: 1133–49.

Turner, G. 1969. Thermal Histories of Meteorites by the 39Ar-40Ar Method. In *Meteorite Research*, edited by P. H. Millman, 407–417. Dordrecht: Springer Netherlands.

Turner, G., Enright, M. C., and Cadogan, P. H. 1978. The Early History of Chondrite Parent Bodies Inferred from Ar-40-Ar-39 Ages. In *Proceedings Lunar and Planetary Science Conference 9th*, 989–1025. New York: Pergamon Press.

Van der Pluijm, B. A., and Marshak, S. 2004. *Earth Structure: An Introduction to Structural Geology and Tectonics*. Dubuque, Iowa: WCB/McGraw-Hill.

van Niekerk, D., and Keil, K. 2011. Metal/Sulfide–Silicate Intergrowth Textures in EL3 Meteorites: Origin by Impact Melting on the EL Parent Body. *Meteoritics & Planetary Science* 46: 1484–97.

Vernon, R. H. 2018. *A Practical Guide to Rock Microstructure*. Cambridge: Cambridge University Press.

Walsh, K. J. 2018. Rubble Pile Asteroids. *Annual Review of Astronomy and Astrophysics* 56: 593–624.

Wlotzka, F., and Otto, J. 2001. Euhedral Crystals in Interstitial Pores of the Baszkówka and Mt. Tazerzait L5 Chondrites. *Geological Quarterly* 45: 257–262.

19455100, 0, Downloaded from https://onlinelibrary.wiley.com/doi/10.1111/maps.70246 by ALEX RUZICKA , Wiley Online Library on [09/11/2026]. See the Terms and Conditions (https://onlinelibrary.wiley.com/terms-and-conditions) on Wiley Online Library for rules of use; OA articles are governed by the applicable Creative Commons License

Woodcock, N. H., and Naylor, M. A. 1983. Randomness Testing in Three-Dimensional Orientation Data. *Journal of Structural Geology* 5: 539–548.

Wright, S. I., Nowell, M. M., and Field, D. P. 2011. A Review of Strain Analysis Using Electron Backscatter Diffraction. *Microscopy and Microanalysis* 17: 316–329.

Xie, X., and Chen, M. 1997. Shock-Produced Vapor-Grown Crystals in the Yanzhuang Meteorite. *Science in China Series D: Earth Sciences* 40: 113–19.

Zeuch, D. H., and Green, H. W., II. 1984. Experimental Deformation of a Synthetic Dunite at High Temperature and Pressure. I. Mechanical Behavior, Optical Microstructure and Deformation Mechanism. *Tectonophysics* 110: 233–262.

Zhang, D., Jiang, L., Zheng, B., Schoenung, J. M., Mahajan, S., Lavernia, E. J. B., and Lavernia, E. J. 2016. Deformation Twinning (Update). *Reference Module in Materials Science & Meterials Engineering*: 1–24. https://doi.org/10.1016/B978-0-12-803581-8.02878-2.

Zsom, A., Ormel, C. W., Dullemond, C. P., and Henning, T. 2011. The Outcome of Protoplanetary Dust Growth: Pebbles, Boulders, or Planetesimals? *Astronomy & Astrophysics* 534: A73.

SUPPORTING INFORMATION

Additional supporting information may be found in the online version of this article.

Table S1. EBSD map metadata. Includes all LAM, DM, and TM map products.

Table S2. List of abbreviations and acronyms used in this work.

19455100, 0, Downloaded from https://onlinelibrary.wiley.com/doi/10.1111/maps.70246 by ALEX RUZICKA , Wiley Online Library on [09/11/2026]. See the Terms and Conditions (https://onlinelibrary.wiley.com/terms-and-conditions) on Wiley Online Library for rules of use; OA articles are governed by the applicable Creative Commons License